Long-term Performance of Engineered Barrier Systems PEBS

Contract (grant agreement) number: *FP7   249681*

DELIVERABLE (D-N°:D2.3-3-1)

Laboratory tests at the interfaces

First results on the dismantling of tests FB3 and HB4

Author(s):

CIEMAT: M.J. Turrero, M.V. Villar, E. Torres, A. Escribano

UAM: J. Cuevas, R. Fernández, A.I. Ruiz, R. Vigil de la Villa, I. de Soto

Date of issue of this report: **31/10/11**

Start date of project: **01/03/10**   Duration : **48** Months

EURATOM

INDEX

LIST OF FIGURES

LIST OF TABLES

1.   INTRODUCTION

Carbon steel canister is one of the candidate overpack materials of the Engineered Barrier System (EBS). The interaction between carbon steel canister, bentonite used as seal material and groundwater can produce corrosion of carbon steel. If canister corrosion occurs the iron will be in contact with the bentonite affecting its properties, both in terms of the chemical evolution of the pore water and the properties of the bentonite. Corrosion of carbon steel can also cause failure of the canister and release of radionuclides to the bentonite barrier. A significant change of the properties of bentonite should be crucial for the migration of the radionuclides.

There are a number of studies on the corrosion of metals that could be used as canister (Taniguchi et al., 2004) and also studies on the iron-bentonite interaction, but not many studies are focused to the iron-compacted bentonite interaction at the repository conditions (Idemitsu et al., 1993, Smart, 2002) and the associated mineralogical, chemical and physico-chemical transformations of the bentonite (Kamei et al., 1991). Some studies in this sense started in the past NF-PRO integrated project supported by the European Commision (Wilson, 2006, Torres et al., 2009, Torres, 2011) with the objectives of studying the corrosion products generated at the canister/bentonite interface under the repository conditions and establishing how the corrosion in these conditions affects the properties of the bentonite.

To tackle the objectives on the corrosion processes in the context of NF-PRO project experiments in cells containing the materials and conditions as close as possible to real ones, with simultaneous heating and hydration (description is given in section 2.1), were designed and assembled in Ciemat. Six cells (FB1 to FB6) were mounted at a time, starting on august 2006. All of them were mounted and run in the same way, except for Cell FB6, in which no hydration took place. The objective of assembling six cells at a time was the sequential dismantling to establish the evolution of the chemical processes at the interface from the unsaturated to the saturated conditions. Two of these cells were dismounted during the NF_PRO project (ENRESA, 2008), after 174 (Cell FB1) and 480 (Cell FB2) days of operation and the results were analyzed in Torres et al. (2009) and Torres (2011). Results showed that, under unsaturated conditions, corrosion phenomena are localized and are related with the distribution of water and solutes in the bentonite and the chloride precipitation in areas close to the canister. The sequence of formation of corrosion products initiates with the formation of ferric hydroxide and evolves to goethite and lepidocrocite. By dehydration, hematite and magnetite are formed. No mineralogical alteration was observed in the tested bentonite, as the corrosion products layer hinders the diffusion of iron.

In the context of the current PEBS project and as a part of the program of sequential dismantling, another cell (FB3) has been dismounted after 1593 days of operation. While previous experiments FB1 and FB2 were considered as short time scale experiments, the FB3 can be considered as a medium term experiment. ***The advance of the results obtained up to now from the dismantling of the cell FB3 is one of the aims of this report***.

On the other hand, cementitious materials are proposed for use as plugs or supporting structures in the various concepts of a repository. The low permeability of concrete, together with its mechanical resistance and chemical properties makes it an adequate constituent of the EBS. Furthermore, from a chemical point of view, the alkaline porewater of concrete decreases the solubility of many radioactive elements.

The European Commision has supported during the last decades scientific research programs focused on chemical processes taking place in the concrete-bentonite interface (ECOCLAY I, II and NF-PRO), since they can affect the feasibility of the barriers. Experiments performed in ECOCLAY I and II projects focused on the stability of the bentonite in contact with concrete pore solutions. Results showed that during the concrete degradation, highly alkaline waters from the concrete will diffuse through the clay barrier. The high pH (12.5 to 13.4) of the pore waters of the concrete contrasts with the pH (7 to 8) of the pore waters in the bentonite. This may produce structural transformations in the bentonite (smectite), dissolution/precipitation of minerals in the bentonite/cement interface and, consequently, changes in the bentonite properties, whose evolution with time may be of great importance to the global performance and safety assessment of the repository. Particularly, the studies carried out with the FEBEX bentonite in contact with concrete (CEM I-SR type) (Huertas, 2000; Leguey et al, 2002, Cuevas, 2005, Cuevas et al., 2006) showed montmorillonite dissolution, precipitation of zeolites (phillipsite-analcime), Mg-smectite, CSH (gels of CSH, tobermorite, girolite) and brucite (Mg(OH)).

During the past NF-PRO integrated project the concrete-compacted bentonite interaction was also studied. To tackle the objectives on it experiments in cells containing the materials and conditions as close as possible to real ones, with simultaneous heating and hydration (description is given in section 2.1) were designed and mounted in Ciemat. Six cells (HB1 to HB6) were mounted at a time, starting on may 2006. All of them were set up and run in the same way. As in the case of the iron-compacted bentonite interface, the objective of assembling six cells at a time was the sequential dismantling to establish the evolution of the chemical processes at the interface from the unsaturated to the saturated conditions. Three of the cells were dismantled during the NF_PRO project, after 196 (Cell HB1), 347 (Cell HB2) and 568 (Cell HB3) days of operation and the main results are in Turrero et al. (2007), Escribano et al. (2008) and Torres et al. (2009).

In the context of the current PEBS project another cell (HB4) has been dismounted after 1610 days of operation, as part of the program of sequential dismantling. ***The advance of the results obtained up to now from the dismantling of the cell HB4 completes the scope of this report.***

2.   EXPERIMENTAL DESCRIPTION

2.1.   Experimental procedure

The tests are performed in cells especially designed for the experiments in the previous project NF-PRO (Enresa, 2008), although similar cells had been used by Martín et al., 2000 and Villar et al. 2005, 2006a and 2008.

They are cylindrical cells with an internal diameter of 7 cm and an inner length of 10 cm. They are made out of Teflon to prevent as much as possible lateral heat conduction. The upper closing of the cells is made by means of a stainless steel plug. Inside this plug there is a deposit in which water circulates at room temperature (25 °C). The bottom part of the cells is a plane stainless steel heater set at a temperature of 100 ºC. In this way, a constant gradient between top and bottom of the sample is imposed. The hydration is made through the upper plug of the cell with water taken from a stainless steel pressurized deposit. The deposit is

periodically weighed to check the water intake. A schematic diagram of the setup and a picture of the cells are shown in Figure 1.
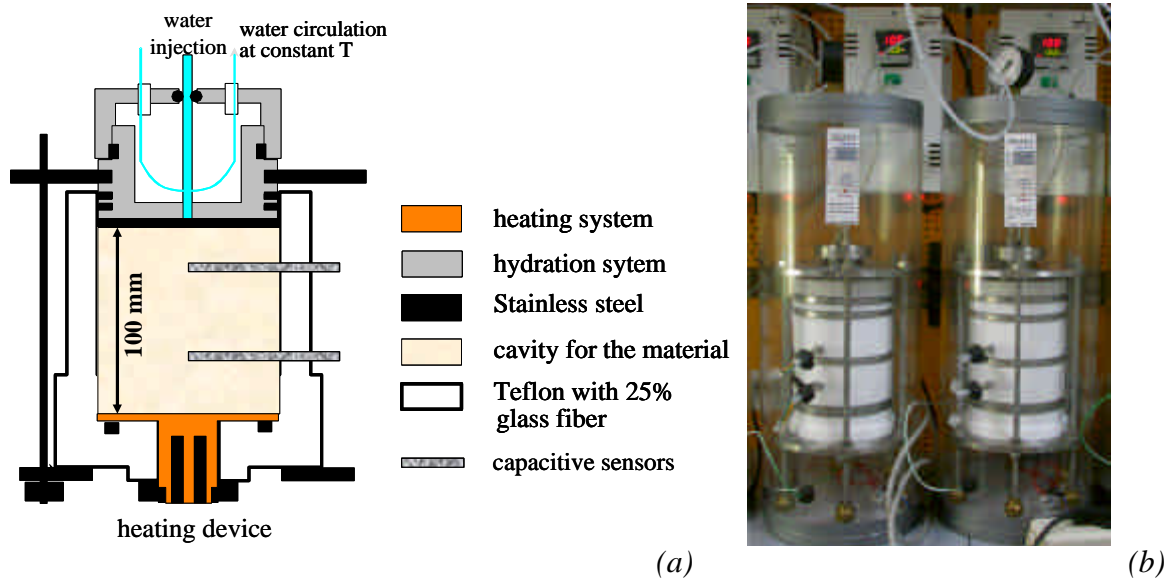
The cells are instrumented with capacitive-type sensors placed inside the clay at two different levels. The transmitters used are Sensirion HMP237, which include a relative humidity (RH) sensor and a temperature sensing element. The RH values are converted to suction values through Kelvin's law.

Blocks of FEBEX bentonite were compacted with its hygroscopic water content (14%) at a nominal dry density of 1.65 g/cm^3 and placed inside the cell. Two kinds of interfaces are investigated, the iron/bentonite interface (in cells FB) and the concrete/bentonite one (in cells HB). The particularities of each of them are given below.

Fe/bentonite interface cells (cells FB)

A uniaxial pressure of 43 MPa was applied to manufacture 86.8-mm long bentonite blocks. At the bottom of the cell, in contact with the heater, 143.4 g of Fe powder were placed, giving rise to an iron layer thickness of 13.0 mm (Figure 2). On top of this, the bentonite block was inserted and a porous filter over it.

Iron powder manufactured by Goodfellow, with a size particle of 60 µm and purity higher than 99% was used for the experiments. Iron powder was used instead of carbon-steal plates to favour the corrosion process at the interface.

Once the assemblage mounted and the sensors connected (at 18 and 74 mm from the heater), the temperature of the heater was initially set to 100°C. The upper cooling was set at room temperature (25ºC). Finally, hydration from the deposit started immediately after assembling the whole system. The deposit was initially pressurized with nitrogen at 5 bars.

The water injected to hydrate the iron/bentonite cells was granite water (Table I) collected every year in the Grimsel Test Site from the BO-ADUS borehole. This borehole is close to the in situ FEBEX experiment, a full-scale experiment to study the processes influencing clay barrier evolution in a granite formation (ENRESA, 2006). The water is alkaline (pH 9.7), reduced, NaCaHCO3- type. The reducing character of water was preserved during hydration. The injection deposit was periodically weighed, and this allowed checking the water intake.
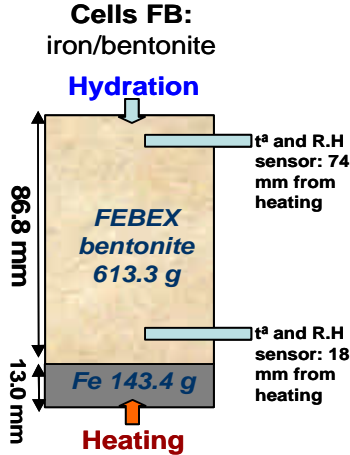
Figure 2.- Diagram showing the configuration and location of sensors in a cell FB to study the iron/bentonite interface.

Table I.- Main chemical species (ppm) in the BO-ADUS groundwater (Grimsel Test Site) used to hydrate FB cells.

Chemical species	Concentration (ppm)
Na^+	8.60 ± 0.06
Ca^{2+}	7.35 ± 0.24
Mg^{2+}	0.40 ± 0.01
K^+	0.88 ± 0.10
SO_4^{2-}	5.90 ± 0.22
Cl^-	0.82 ± 0.04
F^-	4.13 ± 0.10
Alk (HCO_3^-)	24.25 ± 0.37
SiO_2	11.40 ± 0.08
pH	9.7 ± 0.13
Eh	-153 mV

Six cells (FB1 to FB6) were mounted at a time, starting on august 2006. All of them were mounted and run in the same way, except for Cell FB6, in which no hydration takes place. Two of them were dismounted during the NF_PRO project, after 174 (Cell FB1) and 480 (Cell FB2). Another cell was dismounted after 4 years and 6 months of operation (Cell FB3). Other three cells are still running.

Concrete/bentonite interface cells (cells HB)

A uniaxial pressure of 43 MPa was applied to manufacture 71.3-mm long bentonite blocks. At the bottom of the cell, the bentonite block was inserted just in contact with the heater. On top of this, a 30-mm thick concrete block was placed, hydration occurring through the concrete block (Figure 3).

4
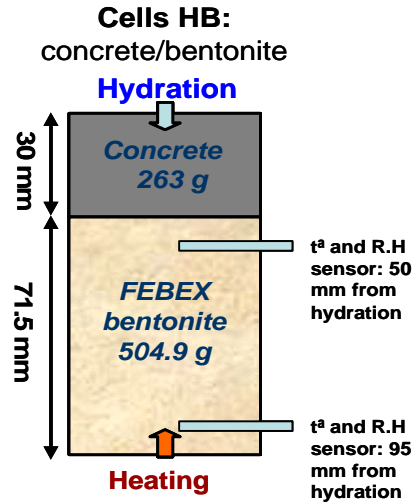
Figure 3.- Diagram showing the configuration and the location of sensors in a cell HB to study the concrete/bentonite interface.

The cementitious materials that are being tested for repository designs are based on sulforesistant ordinary Portland cement (CEM I-SR). This type of concrete was used in the ECOCLAY and NF-PRO projects, and in the experiments actually in course in the PEBS project. The concrete used was manufactured at CIEMAT following the recipe by CSIC-Torroja CEM-SR1 (Hidalgo et al, 2003). Main components of concrete are in Table II.

Table II.- Chemical composition (%) of the concrete CEM-SR1 used in the concrete/bentonite experiments (cells HB).

Chemical composition (%)	SiO_2	Al_2O_3	Fe_2O_3	CaO (total)	MgO	SO_3	Na_2O	K_2O	CaO (free)
CEM I R/SR 42.5 N	19.6	4.43	4.27	64.5	0.95	3.29	0.11	0.28	1.92

The dry density of the concrete was on average 2.22 ± 0.01 g/cm^3 and its initial water content was 2.6 ± 0.8 %. The hydraulic conductivity of samples of concrete was measured in a constant head permeameter at room temperature and an average value of $1.5 \cdot 10^{-11}$ m/s was determined. After saturation the water content of the concrete specimens was on average 6.4 ± 0.6 %. The specific weight of the solid particles was 2.54 g/cm^3.

Once the assemblage set up and the sensors connected (at 50 and 95 mm from the hydration), the temperature of the heater was initially set at 100°C. The upper cooling was set at room temperature (25ºC). Finally, hydration from the deposit started immediately after assembling the whole system. The deposit was initially pressurized with nitrogen at 5 bar. The water injected to hydrate the concrete/bentonite cells is a synthetic clay water obtained from the analysis of a Spanish reference clayey formation (Turrero et al., 2001, 2006) and its chemical composition is given in Table III. The deposits were periodically weighed, and this allowed checking the water intake. Six cells were mounted at a time, starting on 25/5/2006. All of them were set up and run in the same way. Three of them were dismantled during the NF_PRO project, after 196 (Cell HB1), 347 (Cell HB2) and 568 (Cell HB3) days of operation. Another cell was dismounted after 4 years and 5 months (1610 days) of operation (Cell HB4). Other two cells are still running.

Table III.- Main chemical species (M) in the synthetic water obtained from the Spanish Reference Argillaceous Formation used to hydrate HB cells.

Chemical species	Concentration (M)
Fe	1.1E-05
Na	1.3E-01
K	8.2E-04
Ca	1.1E-02
Mg	8.2E-02
Si	2.7E-04
SO_4^{2-}	7.0E-02
Cl^-	2.3E-02
HCO_3^-	1.8E-03
pH= 7.54	

2.2. Materials: FEBEX bentonite properties

The FEBEX bentonite was extracted from the Cortijo de Archidona deposit (Almería, Spain) and the processing at the factory consisted on disaggregation and gently grinding, drying at 60 °C and sieving by 5 mm. The physico-chemical properties of the FEBEX bentonite, as well as its most relevant thermo-hydro-mechanical and geochemical characteristics obtained during the projects FEBEX I and II are summarized in the final reports of the project (ENRESA, 2000, 2006). A summary of the results obtained is given below.

The montmorillonite content of the FEBEX bentonite is above 90 wt.% (92 ± 3 %). The smectitic phases are actually made up of a smectite-illite mixed layer, with 10-15 wt.% of illite layers. Besides, the bentonite contains variable quantities of quartz (2±1 wt.%), plagioclase (3 ± 1 wt.%), K-felspar (traces), calcite (1 ± 0.5 wt.%), and cristobalite-trydimite (2 ± 1 wt.%).

The cation exchange capacity is 102 ± 4 meq/100g, the main exchangeable cations being calcium 35 ± 2 meq/100g, magnesium 31 ± 3 meq/100g and sodium 27 ± 1 meq/100g. The predominant soluble ions are chloride, sulfate, bicarbonate and sodium.

The external specific surface area is 61 ± 2 m^2/g and the total specific surface area is about 725 m^2/g.

The saturated hydraulic conductivity of compacted bentonite samples is exponentially related to their dry density. For a dry density of 1.65 g/cm^3 the saturated permeability of the bentonite is 3.5·10^{-14} m/s at room temperature, either with granite or deionised water used as percolating fluid. The temperature increase results in an increase in permeability, as well as the use of saline water as percolating fluid.

The swelling pressure of compacted samples is also exponentially related to the bentonite dry density, and when the bentonite at dry density of 1.65 g/cm^3 is saturated with deionised water at room temperature, the swelling pressure has a value of about 8 MPa. Saturation with granite water gives similar values, whereas temperature causes a decrease of them, as well as the use of saline water.

The retention curve of the bentonite was determined in samples compacted to different dry densities at different temperatures. The volume of the samples remained constant during the determinations, since they were confined in constant volume cells. Following an approach

similar to that presented by Sánchez (2004) to fit the data from these laboratory determinations, the empirical Equation 1 can be obtained:

$$w = \left(\left(b \cdot n^{c} \cdot e^{-\alpha(T-T_0)} \right) \cdot \left[1 + \left(\frac{s}{P_0 \cdot e^{-\eta(n-n_0)} \cdot e^{-\alpha(T-T_0)}} \right)^{\frac{1}{1-\lambda_1}} \right]^{-\lambda_1} \right) \cdot \left(1 - \left(\frac{s}{P_{\sec}} \right)^{\lambda_2} \right) \cdot \left(S_{lm} - S_{lr} \right)$$

[1]

where w is the water content in percentage, n and n_0 the porosity and reference porosity, s the suction in MPa, T and T_0 the temperature and reference temperature in ºC, S_{lm} and S_{lr} the liquid degree of saturation and liquid residual degree of saturation, P_0, $P_{\sec}$, λ_1 and λ_2 parameters to define the retention curve at reference temperature and porosity, and b, c, α and η fitting parameters to take into account the influence of temperature and porosity. The values of parameters are indicated in Table IV. The differences between measured values and the estimated values using Equation 1 are smaller than 2% in terms of water content.

Table IV.- Values of parameters in Equation 1

b	c	P (MPa)	λ_1	λ_2	η	n_0	α	T_0 (°C)	$P_{\sec}$ (MPa)	S_{lm}	S_{lr}
145	1.9	25	0.2	1.1	20	0.4	0.0015	20	1000	1.0	0.01

2.3.   Evolution of thermo-hydraulic (TH) parameters during the tests

2.3.1   *Relative Humidity and temperature*

Fe/bentonite interface cell FB3

The sensors were placed at 18 and 74 mm from the heater and recorded an initial relative humidity (RH) of 50%. Figure 4 shows the evolution during operation of relative humidity and temperature inside the bentonite for the FB3 cell. The sensor closest to the heater recorded a steady temperature of 90°C, whereas the sensor placed closest to the hydration surface recorded an initial temperature of 40°C that tended to increase over time. After approximately 1000 h the upper sensor recorded relative humidities about 100%. The sensor closest to the heater recorded an initial relative humidity decrease to values around 20%, indicating the desiccation of the bentonite near the heater and the movement of water vapour either to cooler zones in the bentonite or outside the cell (through the sensors' ports). This initial RH decrease was followed by a slow recovery. The recording of the relative humidity sensors in all the cells (dismantled or not) is shown in Figure 5 (only up to 700 days). The pressurization of the hydration deposits usually triggered a subsequent increase of the relative humidity, what suggests that during the intermediate periods the pressure in the deposits decreased as much as not to be enough for saturation to take place.
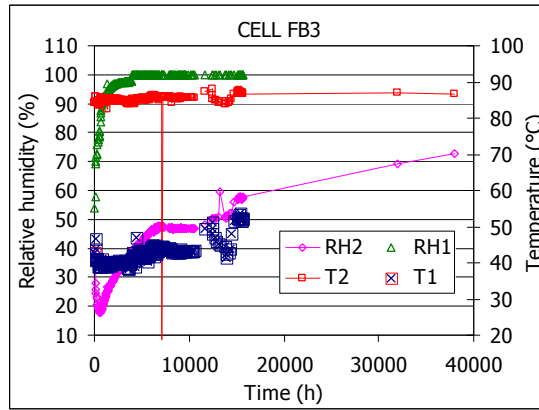
Figure 4.- Evolution of relative humidity (RH) and temperature (T) inside the bentonite in cell FB3 (sensor 1 placed at 18 mm from the heater and sensor 2 at 74 mm).
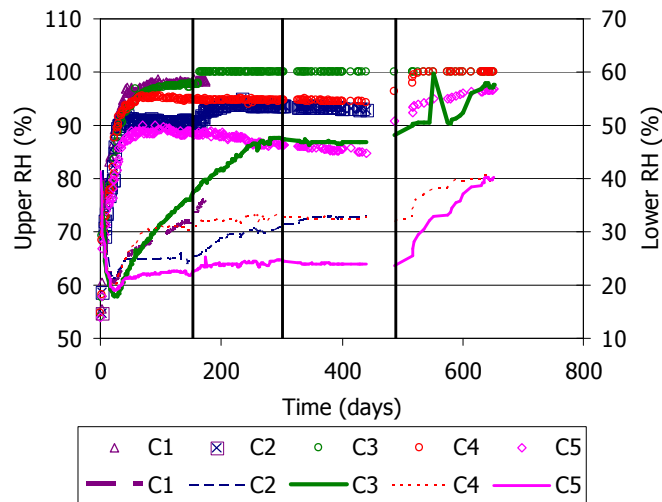
Figure 5.- Evolution of relative humidity in cells FB 1 to 5. Symbols correspond to the upper sensors and lines to the lower ones. The vertical lines indicate pressurisation of the deposits.

Concrete/bentonite interface cell HB4

The sensors were placed at 5 and 60 mm from the heater and recorded an initial relative humidity (RH) of 50%. Figure 6 shows the evolution during operation of relative humidity and temperature inside the bentonite for the HB4 cell. The sensor closest to the heater recorded a steady temperature of 85°C, whereas the sensor placed closest to the hydration surface recorded an initial temperature of 45°C. Very soon after the beginning of the test (a few days) the upper sensor recorded relative humidities about 100%. The sensor closest to the heater recorded an initial relative humidity decrease to values around 35%, indicating the desiccation of the bentonite near the heater and the movement of water vapour either to cooler zones in the bentonite or outside the cell (through the sensors' ports). This initial RH decrease was followed by a recovery, which reached values higher than initial and much higher than in the case of the FB3 cell. This could be caused by the transport of liquid water around the concrete block (which was not sealed to the cell wall) and along the cell' wall towards the sensors' cables. Consequently, this increase in relative humidity would not imply an actual increase in the overall water content of the clay, but just a local increase in the

8

areas around the sensors. This is particularly clear after pressurization of cell HB4, which triggered a sudden, sharp increase in the RH measured by the lower sensor, as observed in Figure 7, where the recordings of the relative humidity sensors for all the cells are plotted (only up to 600 days). The deposits were not pressurized again and, in the long term, the relative humidity of the lower sensors tended to decrease, what suggests that the pressure in the deposits decreased as much as not to be enough for saturation to take place. The low permeability of concrete would have made this effect more relevant. Evaporation through the sensors' ports could have contributed to the overall decrease in relative humidity.
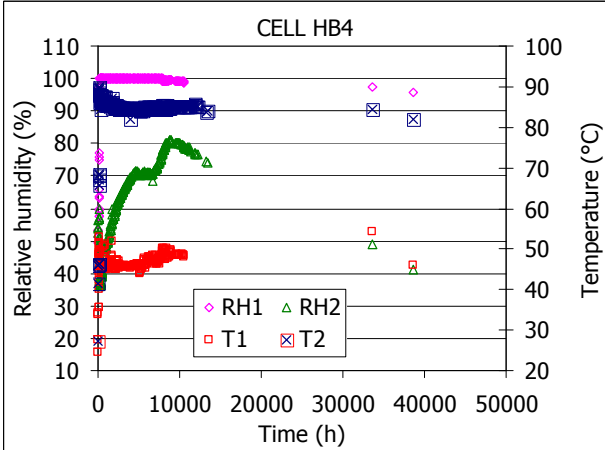
Figure 6.- Evolution of relative humidity (RH) and temperature (T) inside the bentonite in cell HB4 (sensor 1 placed at 5 mm from the hydration and sensor 2 at 60 mm)
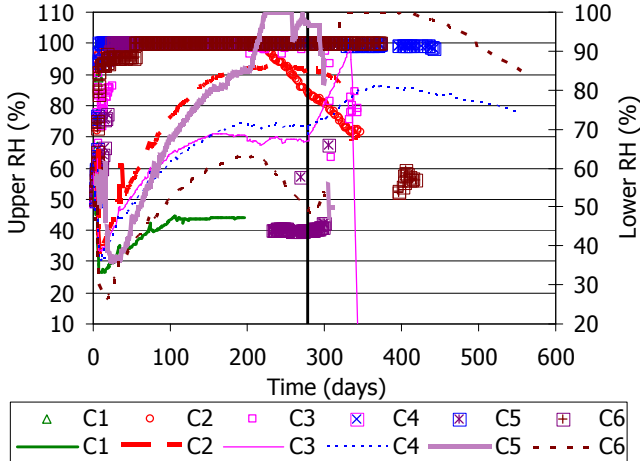
Figure 7.- Evolution of relative humidity in cells HB 1 to 6. Symbols correspond to the upper sensors and lines to the lower ones. The vertical line indicate pressurisation of the deposits

2.4. Dismantling

Cells FB3 and HB4 were dismantled after 4.4 and 4.5 years, respectively. Figure 8a shows an image of the concrete (light top) and bentonite (brown bottom) blocks after dismantling cell HB4. A careful look at the image allows recognize the hydration front on the bentonite. Figure 8b shows the corrosion products after dismantling cell FB3.
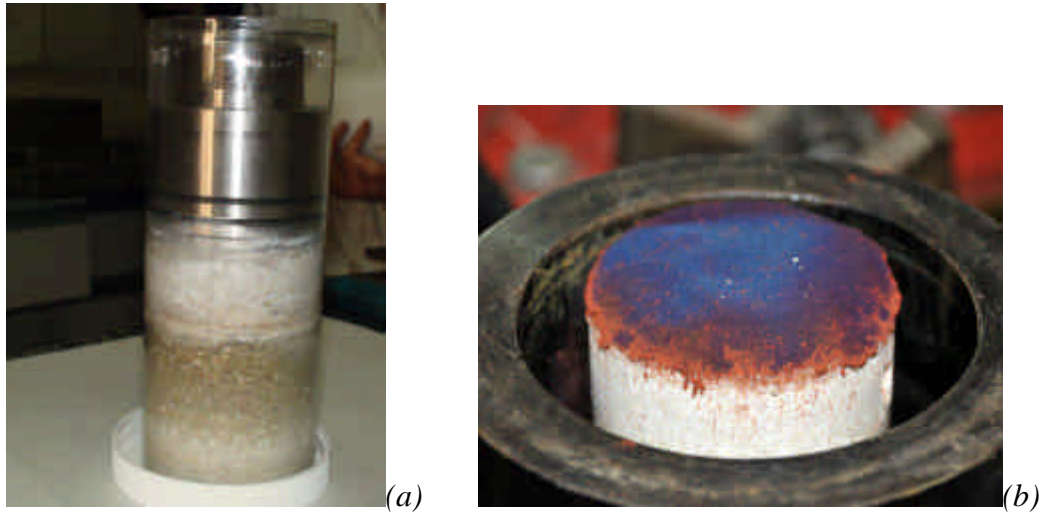
Figure 8.- (a) Image of Cell HB4, dismantled on October 2010; light upper part corresponds to concrete and the darker areas correspond to bentonite; (b) Image of iron in contact with the heater of Cell FB3, dismantled on December 2010.

Once dismantled, three types of samples were analyzed (Figure 9): (1) the precipitates found at the concrete/bentonite and iron/bentonite interfaces and some millimetres far away from the interface; (2) bentonite samples at different distances from the interface, named hydration zone, intermediate zone, heating zone and interface, and (3) concrete and iron sections themselves.
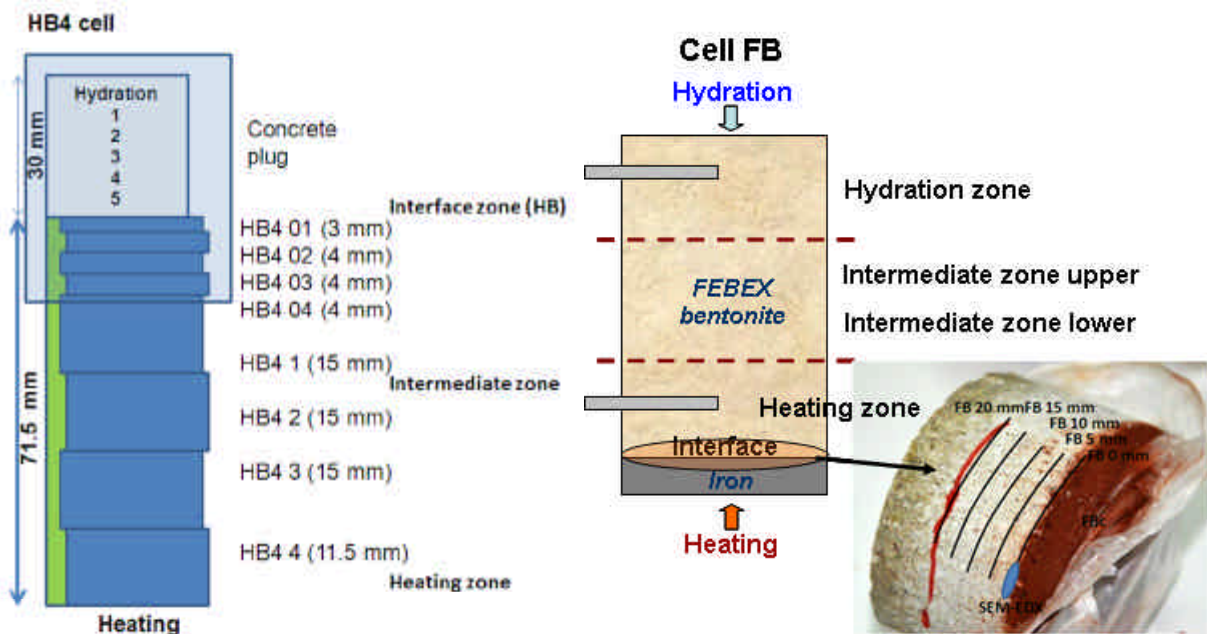
Figure 9.- Left: Sampling of HB4 cell. Square shaded area was preserved for detailed sampling of the concrete and the interface and special cut and resin embedment was made. Right: Sampling of FB3 cell. Picture shows the detailed sampling at the interface.

Iron/bentonite interface cell FB3

A detailed sampling was performed by scrapping the compacted bentonite every 5 mm from the iron interface up to 20 mm length (Figure 9). A chip of the iron-bentonite contact was collected also for a SEM-EDX study, which is equivalent to the FB0 sample in Figure 9. FBC sample is part of hard crusts found in the red layer in the photograph. FBC and FB0 samples were very small samples (< 0.5 g) and 0.1 g was grinded for its analysis in a special powder diffraction mount for very small samples using a 0 background silicon wafer as sample host. The remaining samples of about 1 g were grinded in a Zircon microball mill (RETSCH MM200) and studied for different techniques.

Concrete/bentonite interface cell HB4

HB4 cell was dismantled with the aim to preserve the concrete/bentonite interface. Then the 30 mm piece of concrete and 15 mm of bentonite were wrapped together and isolated from the ambient laboratory with a textile adhesive tissue, a parafilm layer. The remaining part of the compacted bentonite cylinder was cut in four sections as can be seen in Figure 9. A detailed sampling of the 15 mm bentonite interface and the cement matrix of the concrete was performed also for mineralogical and microscopy studies and geochemical characterization.

2.5.   Methods of postmortem analysis

2.5.1   THM analysis

At the end of the tests, the cells were dismantled and the clay blocks extracted. Once extracted, the bentonite columns were sawed in cylindrical sections used for the different determinations.

The gravimetric water content (w), defined as the ratio between the mass of water and the mass of dry solid, was determined by oven drying at 110 °C for 48 hours. Dry density (ρ_d) is defined as the ratio between the mass of the dry sample and the volume occupied by it prior to drying. The volume of the specimens was determined by immersing them in a recipient containing mercury and by weighing the mercury displaced, as established in UNE Standard 7045 "Determination of soil porosity".

For the mercury intrusion porosimetry (MIP) and the physisorption tests samples of sizes lower than 3 cm^3 were cut and lyophilized in a Telstar LioQuest equipment for 24 h at a temperature of -50°C under a vacuum of 0.2 mbar so that to eliminate the water in the pores. The porosimeter used was a Micromeritics AutoPore Series IV 9500, which applied a maximum injection pressure of 33000, what allowed the exploration of pore sizes between 0.003 and 360 µm. The equipment used for the physisorption tests was a Micromeritics ASAP 2020.

The swelling capacity tests were performed in standard oedometers. The specimen (height 1.20 cm, diameter 3.81 cm), contained in the oedometer ring, was confined between two porous stones located at the lower and upper parts. Once in the oedometer, a vertical pressure of 0.5 MPa was applied to the samples. Immediately afterwards, the samples were flooded with water at atmospheric pressure from the bottom porous plate. The swelling strain experienced by the specimens upon saturation was recorded as a function of time until

stabilization. The relation between the increase in final length undergone by the sample in equilibrium with the load applied and its initial length gives the strain experienced by the material on saturating (ε), the negative values indicating swelling strains. The final result is, therefore, the percentage of vertical strain of a sample of a given initial dry density and water content on saturating under a fixed vertical pressure. The tests were performed at room temperature. Intact samples were used to perform this determination. The specimens were just trimmed to fit the ring of the oedometer cell, their dry density and water content being preserved as they were when the TH treatment finished.

For determination of the swelling pressure of the compacted bentonite, oedometer frames and conventional oedometric cells were used. The sample is confined in a ring preventing it from deforming laterally, and between two porous stones at its upper and lower surfaces. The piston of the cell, which is adjoined to the upper porous stone, is in contact with the loading ram, whose displacement may be accurately measured by means of a dial gauge. The sample can be loaded via the ram by means of the system of levers of the oedometric frame on which the cell is located. To determine the swelling pressure, the specimen is saturated with water from the lower porous stone and vertical loads are applied to prevent deformation. With this system the pressure exercised by the sample is determined indirectly from the load that has to be applied in order for the volume of the sample to be kept constant during saturation. The swelling pressure is the vertical pressure needed to hinder any deformation in the saturated sample. As in the case of the swelling capacity tests, the specimens for the swelling pressure were obtained by trimming. Deionised water was used to saturate the specimens.

2.5.2 Geochemical characterization

Each of the bentonite zones was used to analyze soluble elements in aqueous extract solutions. Bentonite samples were dried overnight in an oven at 105ºC. They were ground and placed in contact with deionised and degassed water at a solid to liquid ration of 1:8 (5 of clay in 40 mL of water), shaken end-over-end and allowed to react for 24 hours. Separation was made by centrifugation (30 minutes at 12500 rpm) and the supernatant was filtered by a 0.45-µm pore size filter.

Cations in supernatants were analysed by Inductive Coupled Plasma - Optical Emission Spectrometry (ICP-OES) in a Spectro ARCOS spectrometer after acidification of the samples to pH<2 with HNO3 (8 ml/l). Anions were analysed using ion chromatography (Dionex DX-4500i). Total alkalinity of the samples (expressed as HCO3- concentration) was determined by potentiometric titration using a Titroprocessor Metrohm 716 DMS. The analyses were made by means of a specific Dynamic Equivalence point Titration (DET) method. Additional measures of soluble salts were performed at the interface.

To determine the exchangeable cations of the samples, a CsNO3 solution was used to displace the exchangeable cations. Bentonite samples were equilibrated with CsNO3 0.5 N at pH 8.2 at a solid to liquid ratio of 0.25 kg/L. After phase separation by centrifugation, the supernatant solutions were filtered by 0.45 µm and the concentration of the major cations was analysed by ICP-OES.

FTIR spectra of corrosion products, concrete and bentonite samples were obtained in the middle-IR region (4000-400 cm-1) with a Nicolet 6700 with a DTGS KBr detector (resolution 4 cm-1, 40 scans) on KBr-pressed discs in transmission mode.

X-ray diffraction patterns were recorded on random powder samples of bulk bentonite, concrete and iron oxides. Samples were analysed with a PHILIPS X'PERT MPD diffractometer, using a Cu anticatode and a graphite monocromathor at 45 kV and 50 mA. The scan rate used was 1º 2?/min. PHILIPS X'PERT equipment was operated at UAM facilities as well.

SEM-EDS characterization of the samples was done with a SEM JEOL JM-6400 microscope coupled to a dispersive X-ray energy spectrometer X LINK LZ_5. Iron oxide samples were metallised with gold, whereas in the bentonite samples a graphite coating was deposited on them. SEM-EDS equipment operated at UAM was a Hitachi S-3000N microscope and an INCAx-sight analyzer from Oxford Instruments. A polished vertical section of compacted bentonite or the concrete-bentonite interface was used for optical inspection and to analyze a profile of the chemical composition along the column axis as measured by SEM-EDS.

3.   CHARACTERIZATION OF THE FE/BENTONITE CELL FB3

3.1.   Water content and density

Figure 10 shows the water content and dry density along the bentonite blocks at the end of tests FB1 (174 days), FB2 (480 days) and FB3 (1593 days). As expected, the longer the test, the higher the water contents and the lower the dry densities, since hydration implies swelling, which is not completely hindered by the Teflon cells. The water contents near the heater were in all the cases lower than initial and not very different among the three cells, what would indicate that desiccation (i.e. water vapor movement) was quick and persistent and that the liquid water did not reach the bottom of the bentonite column after 1593 days.
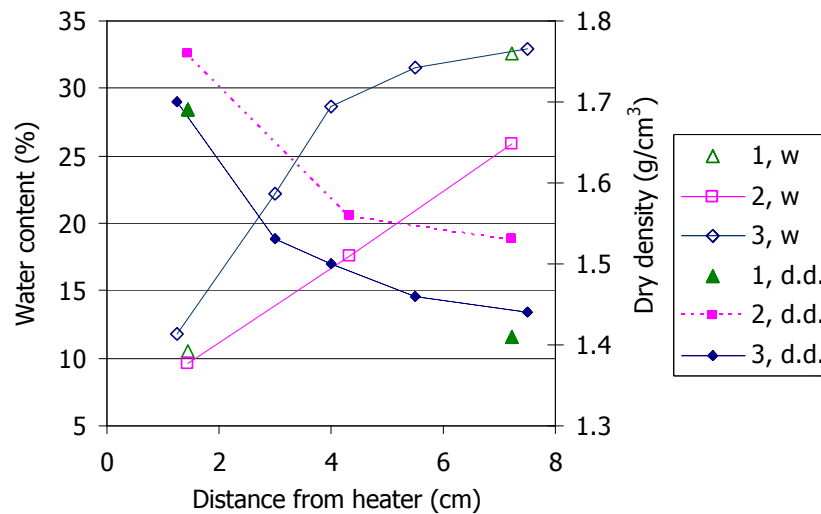
Figure 10.- Final water content (w) and dry density (d.d.) measured along the bentonite blocks at the end of the FB1, FB2 and FB3 tests

The final overall water content of the bentonite blocks can be computed from the difference between the final and initial weights, and the results thus obtained are plotted in Figure 11, where it can be observed that there was a problem with the final weight of cell FB2.
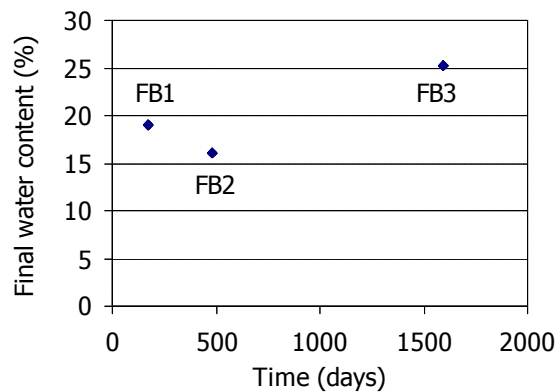
Figure 11.- Final overall water content of the bentonite blocks of cells FB

The water content can be also estimated from the sensors' readings. The relative humidity (RH) and temperature (T) values measured can be converted to suction (s) through the psychrometric law, and related to water content (w) through the empirical Equation 1, that relates suction and water content for the FEBEX bentonite at different dry densities (ρ_d) and temperatures, taking into account the suction computed, the temperature measured, and the porosity. The porosity is computed from the dry density measured in the laboratory at the end of the tests in bentonite close to the sensor. This procedure was successfully applied upon dismantling of the first part of the in situ test at Grimsel (Villar et al., 2006b). The water content values thus inferred are similar to those measured in the laboratory, what fosters the confidence on the sensors' performance (Table V).

Table V.- Water contents measured and inferred from the last sensors' readings in cell FB3

Sensor	RH (%)	T (°C)	s (MPa)	r_d (g/cm3)	w sensors (%)	w measured (%)
FINAL MEASUREMENTS CELL FB1						
1	98.22	41.64	3	1.41	31.7	32.6
2	35.53	83.4	170	1.69	11.6	10.5
FINAL MEASUREMENTS CELL FB2						
1	92.72	48.05	11	1.53	24.6	25.9
2	33.4	83.91	180	1.66	11.3	9.6
FINAL MEASUREMENTS CELL FB3						
1	100	52.16	0	1.44	32.1	32.9
2	72.72	86.60	53	1.62	16.7	17.0

3.2. Pore size distribution and BET surface area

The pore size distribution of bentonite samples from cell FB3 was measured at the end of the test by mercury intrusion porosimetry (MIP) (Campos et al. 2011a). Intact samples with respect to water content and dry density were used after liofilisation. The results obtained are shown in Table VI and Figure 12. The mercury intrusion method allows access to be gained only to the macroporosity (pores smaller than 360 µm) and to part of the mesopores (pores larger than 0.003 µm). An estimation of the percentage of pores actually intruded (column "Total intruded" in Table VI) can be made by comparing the actual void ratio of the samples (computed from their dry density and density of solid particles) and the apparent void ratio calculated from mercury intrusion. The percentage of pores not intruded by mercury included not only those whose sizes were below or above the technique limit, but also those whose entrance pore size was below that value or those isolated, even if the pores themselves were larger. Nevertheless, assuming that the percentage of pores not intruded in a clay corresponds entirely to the micropore size, an estimation of the percentage of micropores can be inferred from the percentage of pores intruded. This was done for all the samples and the percentage of each pore size recalculated, as shown in Table VI.

Table VI.- Mercury intrusion porosimetry results for bentonite samples of test FB3

Reference	ρ_d (g/cm^3)	w (%)	Total intruded (%)	Macro (%)	Macro (nm)	Meso (%)	Meso (nm)	Micro (%)
FB3_1	1.44	32.9	40	23	48135	17	9	60
FB3_2	1.46	31.5	43	27	59323	17	11	57
FB3_3	1.50	28.6	49	31	13738	18	12	51
FB3_5	1.70	11.8	58	37	28535	21	10	42
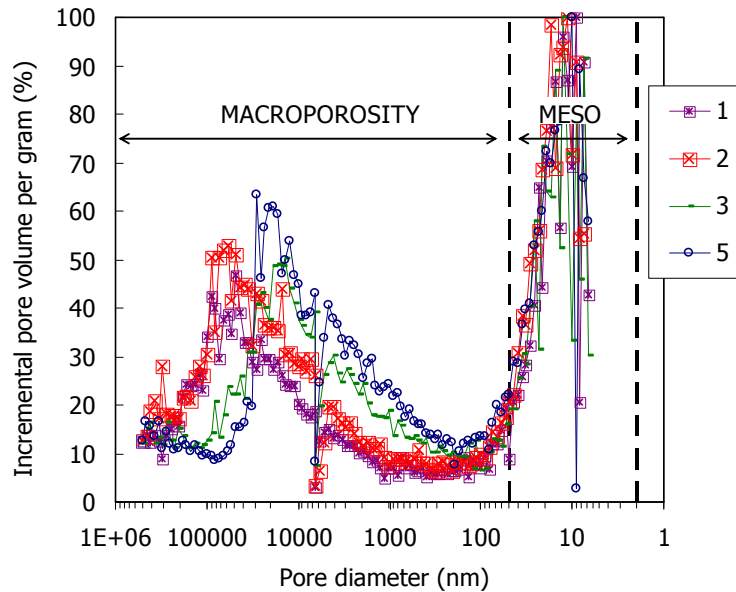
Figure 12.- Mercury intrusion curves of the bentonite at the end of test FB3. Distance from the heater: 7.5 cm (sample 1), 5.5 cm (sample 2), 4.0 cm (sample 3), 1.3 cm (sample 5)

The percentage of pores intruded decreased with water content increase and was below 60% for all the samples, what implied a predominance of micropores, as could be expected for a clay mineral. The increase of water content implied also an increase in the percentage of micropores and a decrease of macropores, while the percentage of mesopores remained constant (Figure 13). The mode of mesopores was similar for all the samples.

These samples were also analysed by physisorption in a ASAP2020 equipment, and the surface areas measured by the BET method are plotted in Figure 14. As has been observed in previous TH experiments (Villar et al. 2008), the surface area decreased clearly towards the heater, and was well correlated with water content. The surface areas measured are similar to that of the untreated FEBEX bentonite, except for the sample closest to the heater. Despite the fact that this sample had a water content not too different from the initial one (12 % vs. 14 %), its BET surface area was much lower, what suggests that temperature is the main cause of the surface area decrease. The *t*-plot micropore volume also increased with water content, in agreement with what was observed in the MIP tests.

Measurements of BET surface just at the interface (red area and crust) and close to it (5 and 10 mm from the red area), as shown in Figure 9, were made in a GEMINI V micrometrics® porosimeter after degassing under N_2 flow during 18 h at 90 ºC (UNE 22-164/94) (Table VII). The specific surface is lower than the values measured towards the hydrated zones of the compacted bentonite (~60 m^2/g) and are in good agreement with those shown in Figure 14 for the zone closer to the heater. As explained above this decrease is presumably due to the temperature increase and dehydration at the heater contact.

16
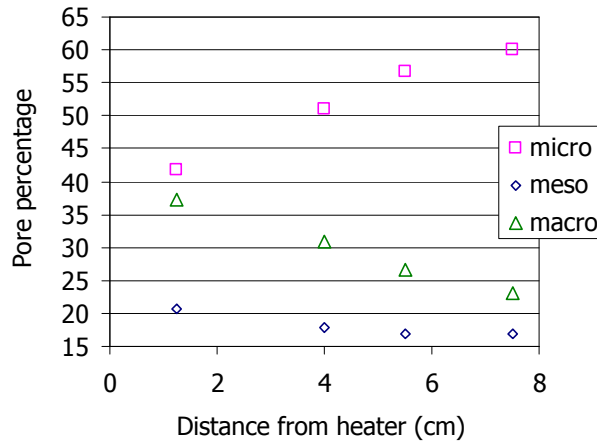
Figure 13.- Pore size distribution of the bentonite at the end of test FB3. Approximate distance from the heater: 7.5 cm (sample 1), 5.5 cm (sample 2), 4.0 cm (sample 3), 1.3 cm (sample 5)
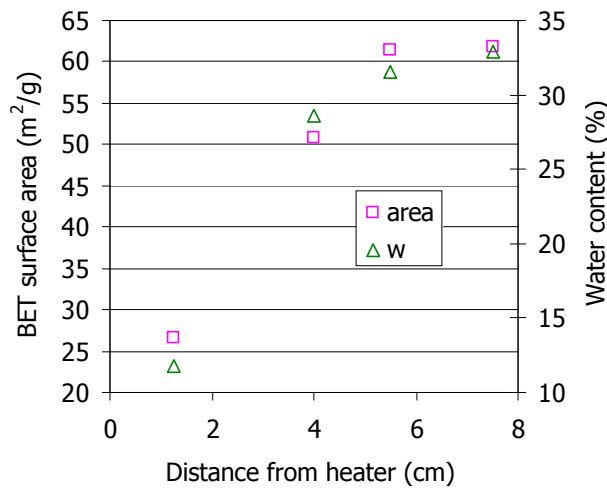
Figure 14.- Measurements of BET surface area by physisorption in samples from test FB3

Table VII.- N_2-BET surface area of samples in the FB interface. Errors of measurements are within ±0.5 m^2/g.

Sample	BET (m^2/g)
FBC (crust)	19.5
FB0 (red)	12.73
FEB5mm	20.93
FB15mm	29.76

3.3. Swelling pressure

The swelling pressure was measured in a sample from cell FB3 taken at 4 cm from the heater (Table VIII, Figure 15). The swelling pressure of this sample was 36% higher than expected for an untreated sample of FEBEX bentonite of the same dry density, but inside the expected range of variation.

Table VIII.- Swelling pressure (Ps) of samples from cell FB3

Reference	Initial ρ_d (g/cm^3)	Initial w (%)	Initial S_r (%)	P_s (MPa)	Duration (days)	Final w (%)	Final ρ_d (g/cm^3)	Final S_r (%)
FB3_3	1.52	27.3	95	4.5	29	30.6	1.52	106
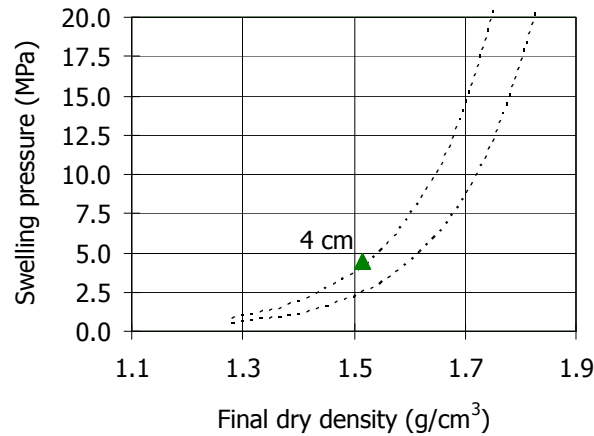
Figure 15.- Swelling pressure of a sample from test FB3 taken at 4 cm from the heater. The lines indicate the expected range of variation for untreated FEBEX bentonite

3.4.   Aqueous extracts

The concentration of soluble elements was analyzed in the four sections represented in Figure 9 from aqueous extracts obtained by mixing dry bentonite and deionised water in a ratio 1:8 (S:L). To understand the distribution of elements along the column comparison with the results obtained from tests FB1 and FB2 is made.

Values obtained from the analysis of the soluble anions are displayed in Table IX. The most relevant transport processes occurring in the cell may be deduced from the behaviour of chloride. The Cl$^-$ distribution (Figure 16) is closely related to the water advection, with the formation of saline fronts moving towards the heat focus. Chloride is easily dissolved when less saline water enters the column and is transported as the hydration front moves to the unsaturated areas, as previously described by Villar et al. (1996), Cuevas et al. (1997) and Fernández and Villar (2010). The advance of Cl$^-$ depends on the duration of the experiment. In the FB1 (174 days) experiment, the maximum chloride content was localized in the intermediate zone. As the hydration front advanced, as in FB2 (480 days), chloride was concentrated at the heating zone and the interface (hottest zone). According to the chemical analysis made on FB3 (1593 days), still unsaturated, Cl$^-$ concentration is also higher at the interface.

High temperature causes the desiccation of the bentonite block and induces the precipitation of salts at the interface (chlorides and carbonates mainly). Salt precipitation may play a relevant role in the performance of the carbon steel canister in the repository. Chloride precipitates are well-known for being hygroscopic. This fact could lead to the formation of very concentrated brines on the surface of the canister, what could favour localized corrosion. EDX analysis of iron powder in contact with bentonite indicated appreciable chloride

concentration (explained in sections below), which can be due to precipitation of chlorides by heating. This fact was also noticed in previous smaller-scale tests (Torres et al., 2009, 2011). Since unsaturated conditions still overcomes at the heater area, advective transport prevails over diffusion as mechanism for salt movement.

Table IX.- Soluble anions concentrations measured in the aqueous extracts (1:8 S/L) for tests FB1, FB2 and FB3.

Cell	Section	mmol soluble anion / 100g dry bentonite	
		Cl^-	SO_4^{2-}
FB1	Hydration zone	0.43	0.02
	Intermediate zone	4.92	0.80
	Heating zone	4.27	0.39
	Interface	0.06	1.69
FB2	Hydration zone	0.11	0.06
	Intermediate zone	0.28	1.79
	Heating zone	5.77	0.96
	Interface	11.94	0.87
FB3	Hydration zone	0.01	0.01
	Intermediate zone upper	0.02	0.04
	Intermediate zone lower	0.01	0.86
	Heating zone	0.01	0.26
	Interface	5.06	1.58
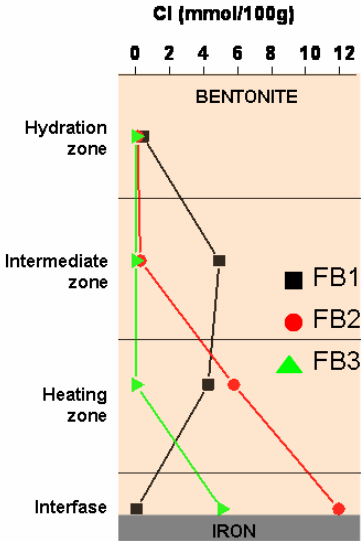
Figure 16.- Chloride concentration along the bentonite block (aqueous extract solid:liquid 1:8)

Transport mechanisms for other chemical species are similar. The SO_4^{2-} content (Figure 17) increases with time due to the solubilization of gypsum. Sulphate is leached from the saturated sections, as shown with chloride. Sulphate front in cells FB1 and FB2 is located in the intermediate zone. The abnormally high value of sulfate found in FB1 test at the interface is possibly caused by the dissolution of some grain of gypsum, not due to the

movement of sulfate towards the heater. However, with time sulphate concentrates at the interface, as in FB3. During first stages the mobility of sulphate is slow, if compared to Cl^-, because of its retention on clay surfaces mainly by electrostatic repulsion (higher ionic charge/radii ratio than Cl^-) (Drever, 1988). With time, the formation of neutral ionic pairs (Mg^{2+}/SO_4^{2-}, Ca^{2+}/SO_4^{2-}), which can move easily between the charged clay surfaces, enhances its movement (Cuevas et al., 1997).
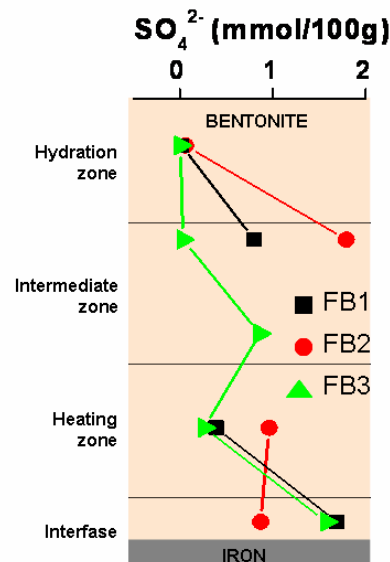
Figure 17.- Movement of sulfates along the bentonite block (aqueous extract solid:liquid 1:8)

Table X shows the average values obtained in the analysis of soluble cations for the tests. With time soluble cations also migrate towards the heater and concentrate at the interface (Figure 18). Sodium decreases close to the hydration source and increases towards hottest zones following a similar trend to chloride in the longest test (FB3). This is not the case of the shortest experiments (FB1 and FB2), in which it seems that other mechanism can influence the sodium distribution. Sodium concentration can be not only controlled by advective transport and dissolution-reprecipitation reactions but also by cation exchange reactions as pointed by Fernández and Villar (2010). Calcium and magnesium behaviour is in agreement with the evolution of sulphate concentrating in the intermediate zones (hydration front) in the shortest tests and in the interface at longer times (FB3). Potassium concentration increases slightly with time. As the rest of soluble cations, it moved towards the heater.

The increase of salinity in the hottest parts of bentonite is possibly caused by the formation of small convection cells generated due to the thermal gradient. At the iron/bentonite interface, water absorbed in bentonite evaporates and moves towards the coldest areas, where it condensates. Liquid water moves again towards the heater. During this movement, the most soluble minerals are dissolved. The hydration front transports salts and saline fronts are generated along the bentonite block. The mobility of these fronts depends on each element. Cuevas et al. (2002) however, proposed that the driving force for salt transport would be the increase of salt concentration on the mesopore "external" water with respect to the "surface-influenced" (anion exclusion) micropore water. The preservation of primitive interfaces between the stacks of montmorillonite lamellae and the macrograins (i.e. quartz) upon saturation can be a proof of the maintenance of preferential pathways for salt migration.

20

Table X.- Soluble cations concentrations measured in the aqueous extracts (1:8 S/L) for the tests FB1 to FB3.

		mmol soluble cation/ 100g dry bentonite			
Cell	Section	Ca^{2+}	Mg^{2+}	Na^+	K^+
FB1	Hydration zone	0.13	0.05	3.48	0.18
	Intermediate zone	0.22	0.11	5.85	0.09
	Heating zone	0.02	0.14	6.95	0.03
	Interface	0.30	0.07	8.59	0.10
FB2	Hydration zone	0.22	0.02	3.29	0.26
	Intermediate zone	0.29	0.14	5.30	0.04
	Heating zone	0.46	0.44	8.5	0.18
	Interface	0.40	0.36	10.8	0.26
FB3	Hydration zone	0.03	0.04	2.49	0.03
	Intermediate zone upper	0.01	0.01	2.16	0.02
	Intermediate zone lower	0.03	0.01	3.42	0.04
	Heating zone	0.03	0.01	2.39	0.02
	Interface	0.29	0.49	7.90	0.31
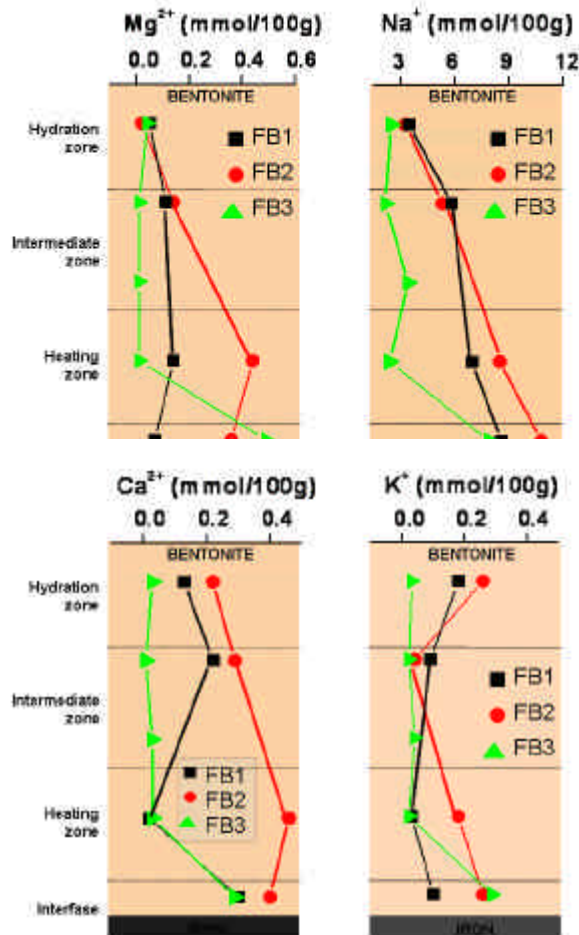
Figure 18.- Cations concentration along the bentonite block for the cell FB3.

3.5. Exchangeable cations

Table XI shows the values of the exchangeable cations measured along the bentonite blocks for the tests. The distribution of exchangeable cations varies along the bentonite column (Figure 19). Magnesium and sodium seem to follow complementary trends, exchangeable sodium increasing close to the hydration surface and dropping near the interface, whereas magnesium decreases in saturated zones and increases near the heater. This fact is particularly clear in the longest test (FB3). Some authors have reported the change in the selectivity coefficients as a function of temperature. According to them, the selectivity coefficient of magnesium increases with temperature, whereas, in the case of sodium, it decreases at higher temperature. Magnesium is released from the interlayers to pore water in the coolest zone and is transported to the hottest zone. Near the heater, magnesium released in saturated areas enters the exchange complex. Magnesium–complexes seem to be more stable at high temperatures than the complexes formed by the rest of the exchangeable cations.

The average value of calcium keeps quite constant in the exchange complex in FB1 and FB2 tests, with the same value obtained for the unaltered FEBEX bentonite (35 meq/100g). However, in FB3 calcium increases in saturated zones (hydration and intermediate) and decreases at the interface, which is interpreted as due to the dissolution of calcite with time, this calcium entering the exchange complex in the saturated areas and precipitating as carbonates in the hottest zone, as magnesium is already occupying the exchange complex at the heater zone.

Similar variations in the exchange complex were described from previous experiments with simultaneous heating and hydration lasted for 8 years in large-scale cells (60 cm) (Fernández and Villar, 2010) where further discussion on the related processes is given.

Table XI.- Exchangeable cations (CsNO3 0.5 N pH 7) measured in the FB1 to FB3 dismantled cells.

| Cell | Section | meq/100g | | | |
		Ca^{2+}	Mg^{2+}	Na^+	K^+
FB1	Hydration zone	35	27	35	3
	Intermediate zone	36	27	34	3
	Heating zone	35	36	26	3
FB2	Hydration zone	38	20	38	3
	Intermediate zone	35	27	35	3
	Heating zone	35	34	28	3
FB3	Hydration zone	40	21	31	2
	Intermediate zone upper	41	20	29	2
	Intermediate zone lower	40	20	27	2
	Heating zone	42	21	27	2
	Interface	26	44	15	3
FEBEX bentonite		35	31	27	3
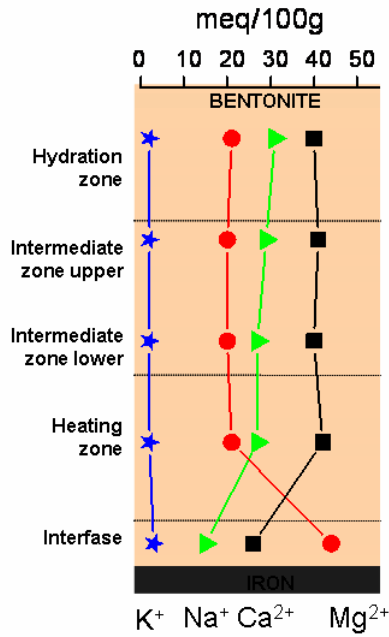
Figure 19.- Distribution of exchangeable cations in the FB3 dismantled after 4.5 years of operation ($CsNO_3$ 0.5N)

The average value of potassium in the exchange complex measured in all samples is 3 meq/100g, which is the same value found for unaltered FEBEX bentonite.

Cation exchange capacity values at the interface samples are shown in Table XII. The procedure for the displacement of cations adapted to use, duplicated, < 0.2 g of sample. The displacement was done with ammonium chloride (0.25 M at pH 7) three times and the obtained solution, once diluted (at least 1:10) was measured by HPLC ion chromatography. The results agree with the general trends described above. Exchangeable magnesium rises close to the interface, and it seems to be related to the increase of layer charge. This fact has to be further confirmed. The increase of Mg towards the hot side was previously observed in several thermal gradient experiments with the FEBEX bentonite (Villar et al., 2008, Fernández and Villar, 2010).

Table XII.- Exchangeable cations for FB3 5 and FB3 15 interface samples (meq/100g)

Sample	Na^+	K^+	Ca^{2+}	Mg^{2+}	SUM
FB3 5 mm	15.4 ± 0.1	3.8 ± 0.1	28.4 ± 0.2	84.4 ± 2.1	132.0 ± 2.2
FB3 15 mm	12.6 ± 0.1	3.7 ± 0.1	31.7 ± 0.3	66.0 ± 0.7	113.9 ± 0.9

3.6.   Mineralogy at the interface

3.6.1 Bulk sample

The mineralogical composition of the bentonite was studied at the different samples illustrated in Figure 9. The composition at the iron corrosion products interface (Table XIII) is very similar to the natural bentonite (Figure 20).

Table XIII.- Mineralogy of the samples collected at the iron-bentonite interface. Qtz: quartz,
Cal: calcite, Pl: plagioclase, Kfs: K-feldspar, Sa:sanidine; Mnt: montmorillonie, Crs:
cristobalite, Hem: hematite. Dt: detected; X: significant (< 5 %); XX: abundant (5 – 10 %);
XXX: major (> 80 %)

Sample	Qtz	Cal	Pl	Kfs	Mnt	Crs	Other reflections
FB0mm	X	-	X	tr	XXX	X	2.69 Å; 3.18, 2.28 (Hem)
FB5mm	X	-	X	tr	XXX	-	
FB10mm	X	X	X	tr	XXX	-	
FB15mm	X	-	X	X	XXX	-	3.30 Å (Sa)
FB20mm	X	tr	X	tr	XXX	-	
FBC	X	-	X	tr	XXX	XX	

The red interface (FB0) contains Fe (III) oxide hematite and also cristobalite. Some XRD peaks were not identified in this sample and the intensities of the bentonite characteristic peaks (as seen in FB20mm) are slightly decreased. Hard crusts in the red interface show an increase in the intensity of the cristobalite peak (4.05 Å) and confirm its presence as part of the mineralogical changes produced in this interface (Figure 20). Dissolution/precipitacion processes of silica at the interface are probably the responsible of the presence of cristobalite at the interface.

3.6.2 Oriented clay films

In order to study the characteristics of the clay fraction (< 2 µm), 0.2 g of bulk powder of several samples were dispersed in distilled water and allowed to sediment in a 250 cm^3 test tube in order to separate > 2 µm size particles. The operation was repeated three times and the supernatant was collected every time to concentrate the < 2 µm size fraction. The obtained suspension was flocculated by adding $MgCl_2$ 0.5 M and centrifuged. The clay was then washed three times with pure alcohol and then dried at ambient laboratory. The amount of clay separated was in the order of 0.1 g, which was suspended in 4 cm^3 of distilled water. Approximately 3 portions of 1 cm^3 suspension were smeared in glass tiles (1.5 x 2 cm) in order to prepare dry films to get air dried oriented clay films, ethylene-glycol oriented clay films and 550ºC oriented clay films (Moore and Reynolds, 1989).

All the studied samples show a complete swelling to 17 Å when they are solvated in ethyleneglycol (Figure 21), and dehydrate to 9.7 Å when they are heated to 550 ºC (not shown). This confirms the quite standard values measured for the cation exchange capacity of the samples, in agreement with their fully smectitic nature.
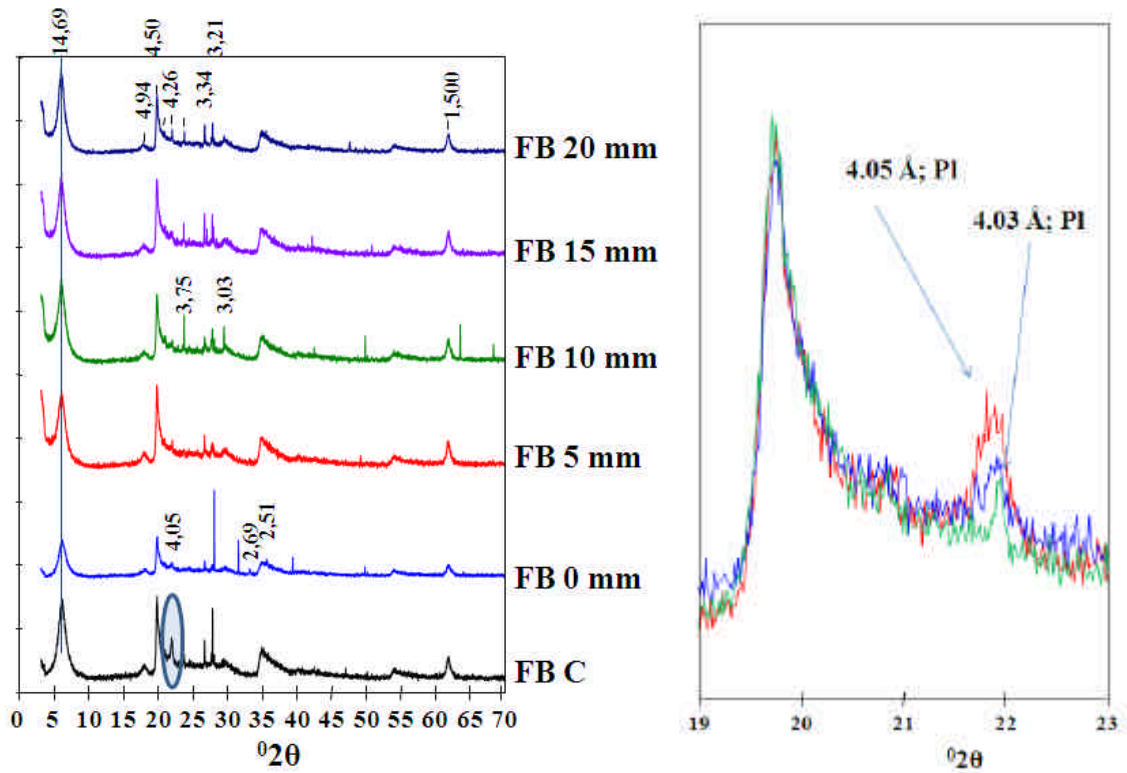
Figure 20.- Left: XRD powder patterns from the iron corrosion products-bentonite interface. Numbers are the peak positions in Å. Right: detail of the XRD random powder cristobalite peak in the indurated crust (red, FBC), compared to FB0mm red sample and FB20mm (green) sample.
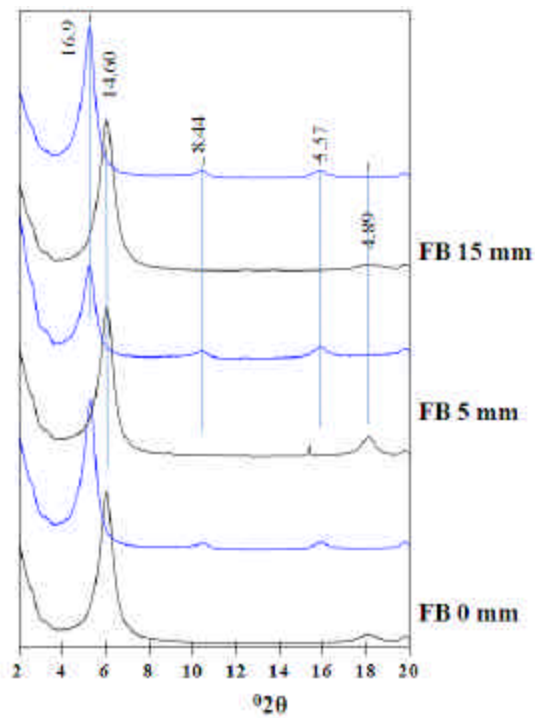
Figure 21.- Clay oriented films XRD patterns. In black: trace of air dried oriented flims. In blue: Ethylene-glycol solvated oriented films. Numbers are the peak positions in Å

3.6.3 SEM data

The observation of the red interface sample by SEM-EDX has confirmed the presence of sub-micrometric (< 1µm size) aggregates of silica within a dense packed materials in the red surface. Fine powdered iron oxides were observed also without evidence of development of crystalline faces. The formation of silica minerals in this relatively dry interface implies some dissolution-precipitation process under alkaline conditions at any time in order to dissolve silica. This process should be followed in the long term experiments. Figure 22 shows several aspects of the FB interface clay fabric.

Dense packed material: Hard crusts

Oxides %	Base	Beads
Na_2O	-	-
MgO	8.08	4.25
SiO_2	60.48	82.61
K_2O	0.45	-
Al_2O_3	20.58	9.69
CaO	0.46	-
Fe_2O_3	9.95	3.45
Total	100	100

Iron in FB interface

Oxides %	FB interface powder	Base
Na_2O	-	-
MgO	6.47	6.93
SiO_2	39.31	67.27
K_2O	0.32	0.60
Cl	0.43	0.37
Al_2O_3	13.90	19.07
CaO	-	0.61
Fe_2O_3	39.55	5.15
Total	100	100

Cristobalite beads in dense clay

Iron oxide powder in FB interface
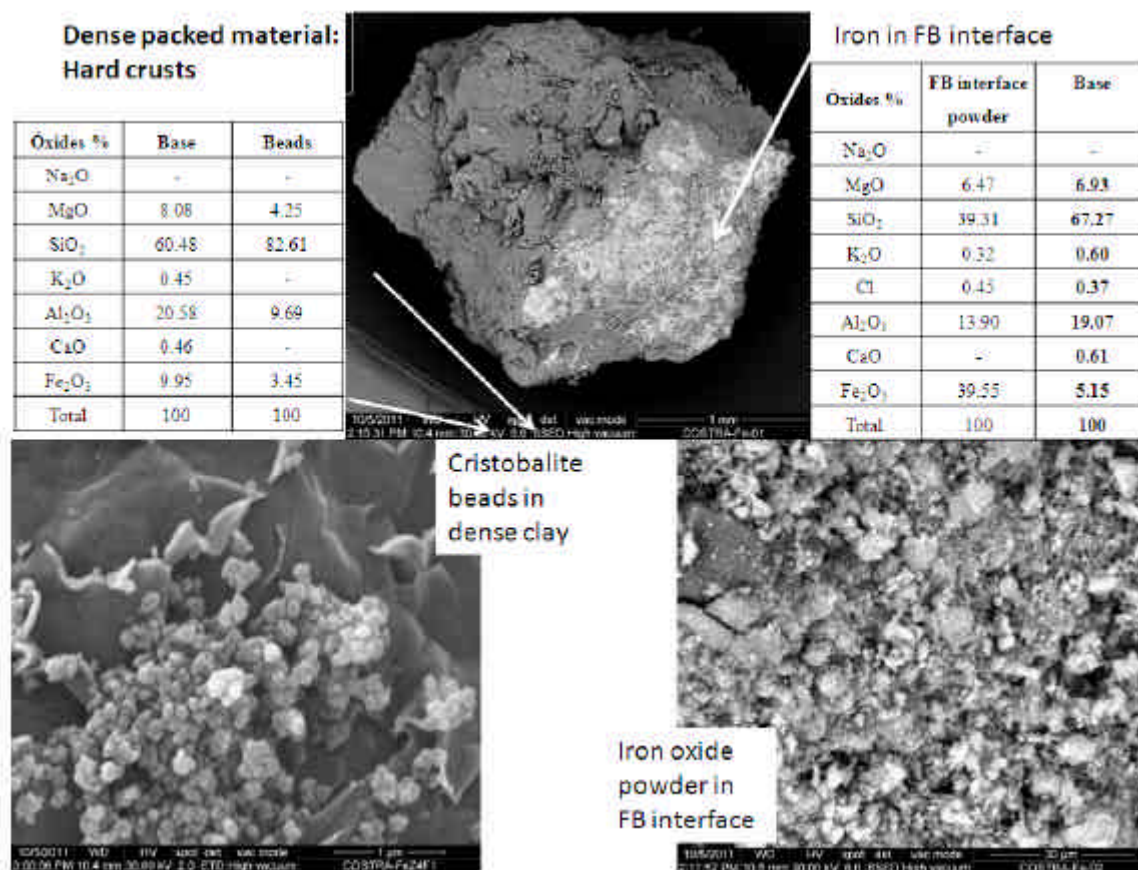
Figure 22.- SEM photographs and EDX analyses in the FB3 iron-bentonite interface. Base analysis corresponds to the clay under the iron oxide or cristobalite deposits.

3.7. Corrosion products

Iron powder was sampled and analyzed based on differences of colour observed when the cell was dismantled, from the interface (red) to the heater (blue) (Figure 8b). The samples were named as interface-red (or FB0, as in Figure 9), which was in contact with the bentonite, blue, which was in contact with the heater and red-brown, placed between red and blue ones. SEM and FTIR spectroscopy were used for the characterization of corrosion products precipitated on the bentonite surface and the iron oxides formed on the surface of the iron powder.

EDX analysis of different points at the interface-red area measured traces of common elements in the composition of bentonite (Table XIV). Furthermore, calcium, chloride and

iron were the other elements measured in different points. The corrosion products layer is not homogeneous at the iron/bentonite interface, and reddish agglomerates were distinguished all over the surface of the bentonite block. Analyses at different zones (Table XIV) evidences variation in the iron content. From the examination of the iron powder in contact with clay, iron oxides were detected on the surface of some discrete particles. Precipitation of calcite due to the high temperature reached at the interface could explain the presence of calcium in corrosion products. However, the content of calcium was irrelevant if compared with the chlorine content. Chloride precipitated on the metal surface could have a relevant role on the initialization of corrosion phenomena, due to its hygroscopic properties.

Identification of corrosion products found on the bentonite surface was performed by means of FTIR spectroscopy. FTIR spectra collected for the interface-red sample (Figure 23a) of the FB3 test shows bands corresponding to akaganeite, lepidocrocite and goethite. Typical band for akaganeite was found at 3458 cm^{-1} and 1095 cm^{-1}, lepidocrocite was placed at 1021 cm^{-1}, whereas the characteristic doublet corresponding to goethite was centered at 897 and 794 cm^{-1}. After SEM observation, the morphology of these oxides is irregular and their size range from few hundred nanometers to microns. Figure 23b shows a spectra corresponding to the bentonite itself at the interface with no presence of alteration.

Table XIV.- EDX analyses at different zones of the interface-red sample, just at the contact of the iron with the bentonite in FB3.

Oxides (%)	Interface 1	Interface 2	Interface 3
Na_2O	0.62	0.53	
MgO	7.75	6.65	2.11
SiO_2	57.69	43.95	11.09
K_2O	1.31	1.14	0.23
Al_2O_3	16.70	12.79	3.52
CaO	1.33	1.20	0.52
FeO	13.23	32.55	81.75
Cl	0.45	0.43	0.33
SO_3	0.61	0.55	

(a)   (b)
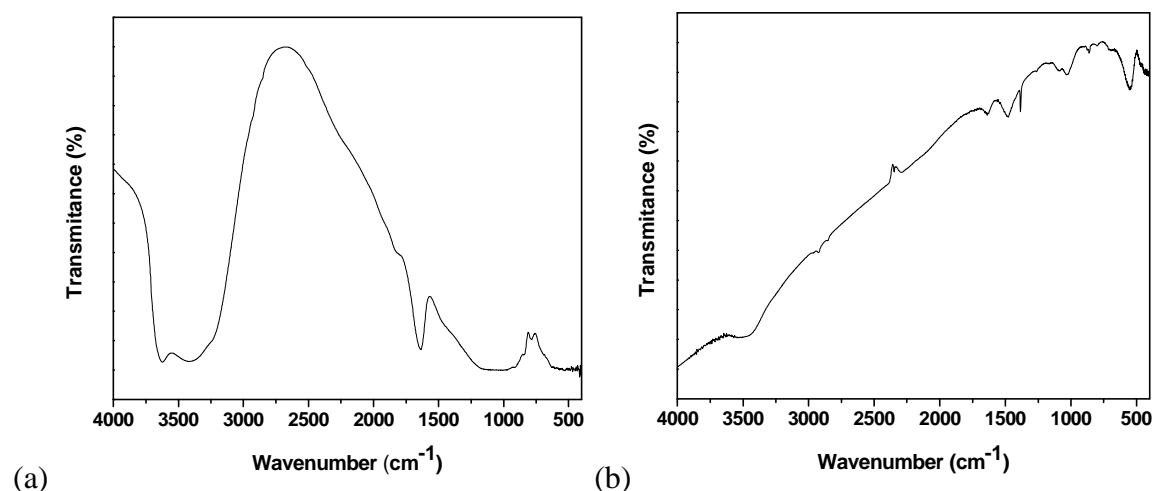
Figure 23.- FTIR spectra recorded (a) for the interface-red sample collected at the iron/bentonite interface (or FB0) and (b) for the bentonite itself at the interface.

As seen in section 3.3 soluble salts determination performed on bentonite samples collected at the iron/bentonite interface indicated that soluble chloride increases just at the interface. Concentration and later precipitation of chlorides at the interface and in the iron powder could explain high chloride contents in the corrosion products in the test. As chloride salts are hygroscopic and are able to adsorb environmental moisture, electrochemical corrosion is due to occur in these zones. The chloride precipitates could initiate localized corrosion phenomena and would explain the presence of akaganeite as part of the corrosion products generated at the interface. Corrosion in this case would occur quite quickly until most of the residual oxygen trapped in the cell is consumed. Typical corrosion products formed during electrochemical corrosion under aerobic conditions are goethite and lepidocrocite.

Figure 24 shows a picture of different points of the red-brown zone and EDX analysis of them. Iron and chlorine are the elements found at this zone. The FTIR spectra recorded for this sample (Figure 25) shows bands corresponding to akaganeite, lepidocrocite, goethite and a doublet typical for hematite. Chlorine has reached inner zones of the iron layer and a sequence of corrosion products probably initiated by the presence of that chlorine, the high temperature and the lack of hydration has been identified.

(a)   (b)
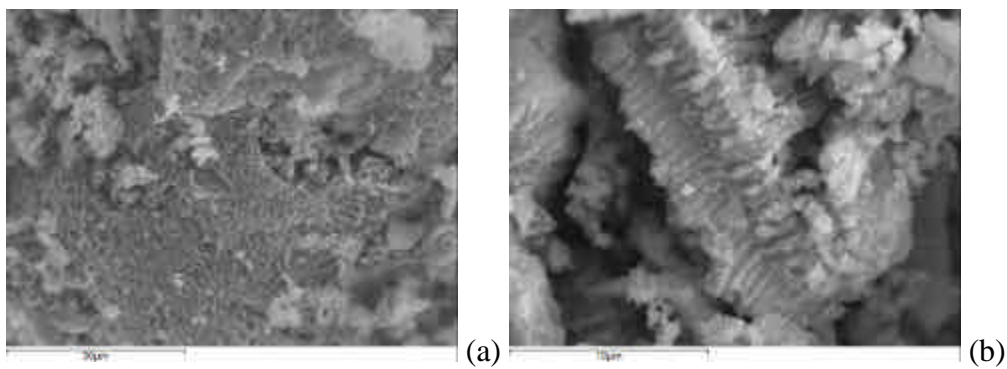
Oxides (%)	Red-brown 1 (a)	Red-brown 2 (b)
FeO	99.49	99.76
Cl	0.52	0.24

Figure 24.- SEM photograph and EDX analyses at different zones of the red-brown sample.
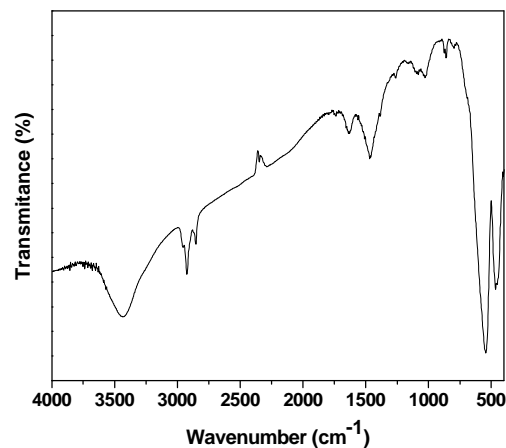
Figure 25.- FTIR spectra recorded for the red-brown sample.

Figure 26 shows a picture of the blue zone as discrete particles and EDX analysis of two different points on them. Iron and silica are the elements found at this zone. The presence of silica is in agreement with the dissolution/precipitation of silica described above. Silica could migrate through the iron layer towards the heater. The FTIR spectra recorded for this sample (Figure 27) shows bands corresponding to lepidocrocite, goethite, $Fe(OH)_2$ and GRs.
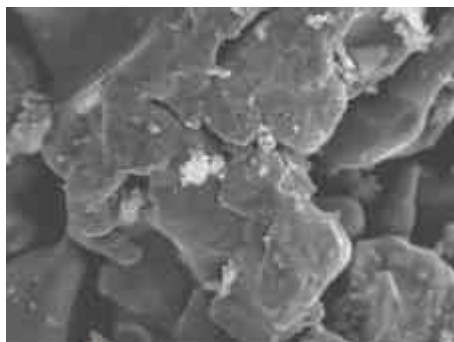
Oxides (%)	Blue 1	Blue 2
FeO	99.68	99.92
SiO$_2$	0.32	

Figure 26.- SEM photograph and EDX analyses at different zones of the blue sample.
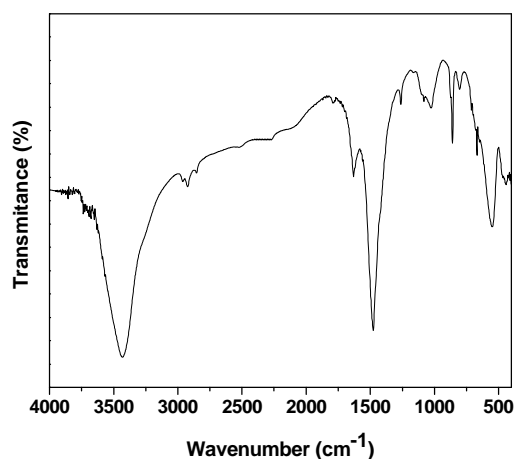
Figure 27.- FTIR spectra recorded for the blue sample.

4. CHARACTERIZATION OF THE CONCRETE/BENTONITE CELLS

4.1. Water content and density

The final distribution of water content and dry density of bentonite in cell HB4 after 1610 days is shown in Figure 28. The water content was very high in the 2-3 cm closest to the concrete surface, but it decreased sharply beyond this area and remained in values only slightly above the initial water content. In the 2 cm closest to the heater the water content was lower than initial. Despite the fact that the duration of the test was similar to that of test FB3, the final water contents measured, as well as the water content computed by weight differences, are much lower in the case of test HB4 (15.6% vs. 25.3%). This could be due to the higher difficulty of liquid water of getting to the bentonite through the concrete block under a low injection pressure (since the water deposits were depressurized).
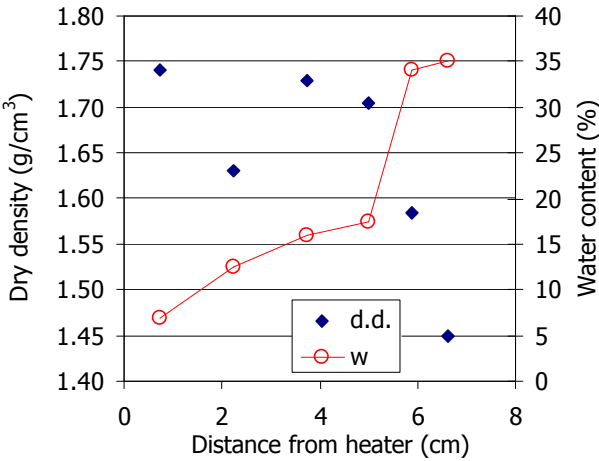
Figure 28.- Measurements of water content and dry density along the bentonite column at the end of test HB4

As in the case of cells FB (see section 3.1 for detailed description of calculations), the final water contents around the sensors have been computed from the sensors' readings (Table XV). The agreement is not as good as for the FB cells.

Table XV.- Water contents measured and inferred from the last sensors' readings in cell HB4

			FINAL MEASUREMENTS CELL HB4			
Sensor	RH (%)	T (°C)	s (MPa)	ρ_d (g/cm^3)	w sensors (%)	w measured (%)
1	95.80	45.96	6	1.45	28.0	34.0
2	41.12	82.12	145	1.69	12.3	6.9

4.2. Pore size distribution and BET surface area in the bentonite

The pore size distribution of bentonite samples from cell HB4 was measured at the end of the test by mercury intrusion porosimetry (Campos et al. 2011b). Intact samples with

30

respect to water content and dry density were used after liofilisation. The results obtained are shown in Table XVI and Figure 29, where the same comments made in section 3.6 apply. It must be pointed out that no samples in contact with the concrete were analyzed, since sample 1 was taken from about 3 cm from the concrete surface and that is why the water content of the samples analyzed is below 18%. Consequently, no conclusions on the effect of the alkaline front on pore size distribution could be drawn from these results.

The percentage of pores intruded was below 60% for all the samples, what implied a predominance of micropores, as could be expected for a clay mineral. Although there is not a significant difference between the four samples analyzed, the percentage of micropores increased towards the heater while the pore mode of macropores decreased, what could be connected to the increase in dry density (Figure 30). The mode of mesopores was the same in all the samples.

These samples were also analyzed by physisorption in an ASAP2020 equipment, and the surface areas measured by the BET method are plotted in Figure 31. As has been observed in previous TH experiments (Villar et al. 2008), the surface area decreased clearly towards the heater, and was well correlated with water content. Except for the samples hydrated (1 and 2), the surface area is lower than that for the untreated FEBEX bentonite.

BET specific surface area was also measured in four samples taken from the first 15 mm of bentonite at the interface zone. It was measured by N_2 adsorption with a Gemini V analyzer from Micromeritics. Specific surface area is almost identical to the original FEBEX bentonite (Table XVII), with a very small decrease at the interface zone that has to be confirmed in the long time experiment.

A concrete fragment was also analyzed at the end of the TH test after liofilisation. Most of the pores are comprised between 1000 and 10 nm (Figure 32), with a mode of 44 nm. A 78% of the total pore volume was intruded by mercury, what points to the existence also of microporosity.

Table XVI.- Mercury intrusion porosimetry results for bentonite samples of test HB4

Reference	ρ_d (g/cm^3)	w (%)	Total intruded (%)	Macro (%)	Macro (nm)	Meso (%)	Meso (nm)	Micro (%)
HB4_1	1.71	17.5	56	25	35165	31	9	44
HB4_2	1.73	15.9	55	26	23165	30	9	45
HB4_3	1.63	12.5	54	32	13731	21	9	46
HB4_4	1.74	6.9	51	31	10023	20	8	49
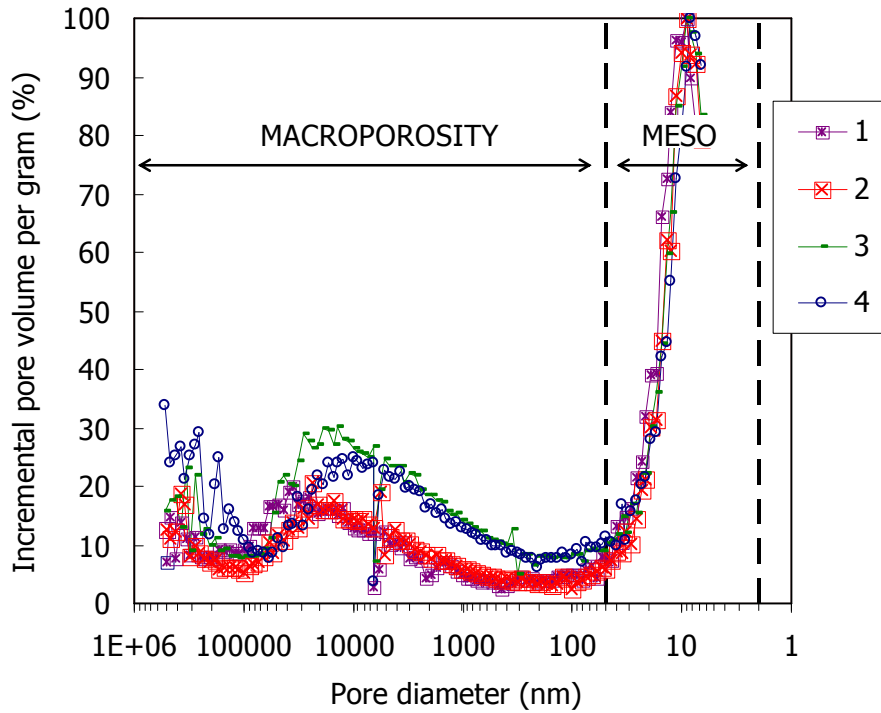
Figure 29.- Mercury intrusion curves of the bentonite at the end of test HB4. Approximate distance from the heater: 5.0 cm (sample 1), 3.8 cm (sample 2), 2.2 cm (sample 3), 0.8 cm (sample 4)
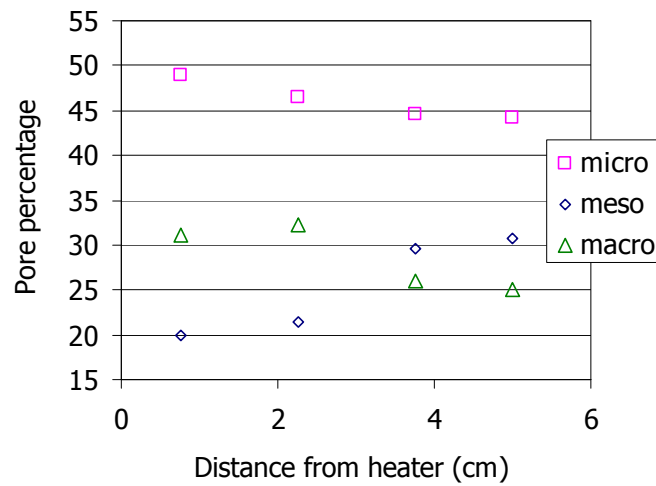
Figure 30.- Pore size distribution of the bentonite at the end of test HB4. Approximate distance from the heater: 5.0 cm (sample 1), 3.8 cm (sample 2), 2.2 cm (sample 3), 0.8 cm (sample 4)
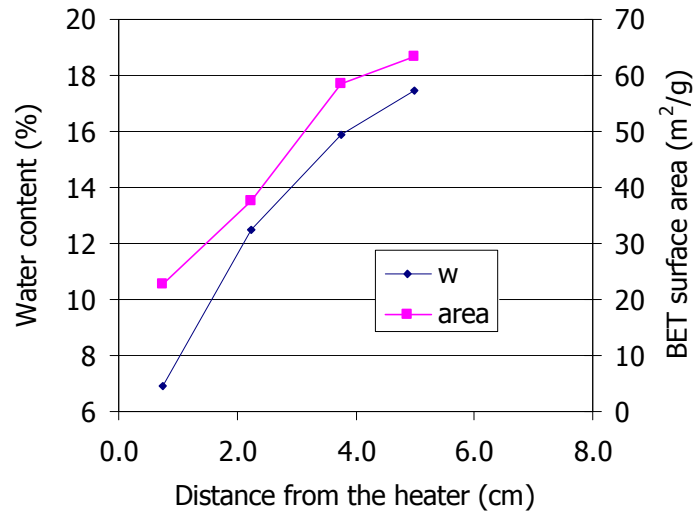
Figure 31.- Measurements of BET surface area by physisorption in samples from test HB4

Table XVII.- N$_2$BET Specific surface measured at the concrete-bentonite interface

SAMPLE	BET (m^2/g)±0.5
HB401 0-3 mm	61.1
HB402 3-7mm	60.9
HB403 7-11mm	63.1
HB404 11-15 mm	62.0
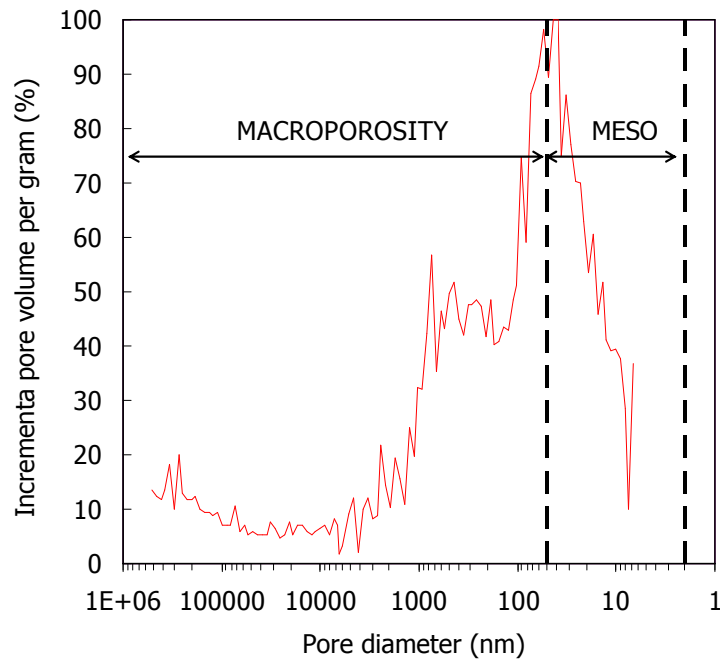
Figure 32.- Pore size distribution of the concrete at the end of test HB4

4.3. Swelling capacity and swelling pressure

The swelling capacity was measured in a sample from test HB1 and the swelling pressure in two samples from test HB4. In all the tests deionised water was used as saturation fluid. The results are shown in Table XVIII and Table XIX, where the values of initial and final dry density (r_d), water content (w), deformation (e), swelling pressure (P_s) and degree of saturation (S_r) are indicated. The values of degree of saturation are higher than 100% because they have been calculated taken the density of water as 1 g/cm^3, what is not so far that of the interlaminar water of smectites. The swelling capacity of the sample closest to the hydration surface (i.e. to the concrete) in cell HB1 was in the range expected. The results of the swelling pressure test in samples from cell HB4 are shown in Figure 33, where the range of expected values for the untreated bentonite is also indicated. The sample closest to the heater had a swelling pressure 44% smaller than expected for an untreated FEBEX sample of the same dry density, whereas the swelling pressure of the sample taken farther from the heater was 25% lower than expected, but inside the expected range of variation. Then, it would be necessary in the longest term experiments to measure both porosity and swelling pressure in a section from the concrete/bentonite interface.

*Table XVIII.- Swelling capacity (**e**) under a vertical strain of 0.5 MPa of a sample from cell HB1*

Reference	Initial r_d (g/cm^3)	Initial w (%)	Initial S_r (%)	ε (%)	Duration (days)	Final w (%)	Final r_d (g/cm^3)	Final S_r (%)
HB1_2	1.51	26.1	90	-9.4	31	39.9	1.38	113

Table XIX.- Swelling pressure (Ps) of samples from cell HB4

Reference	Initial r_d (g/cm^3)	Initial w (%)	Initial S_r (%)	P_s (MPa)	Duration (days)	Final w (%)	Final r_d (g/cm^3)	Final S_r (%)
HB4_2	1.71	15.4	72	8.1	11	27.7	1.69	125
HB4_4	1.71	7.2	33	5.8	11	30.4	1.69	136
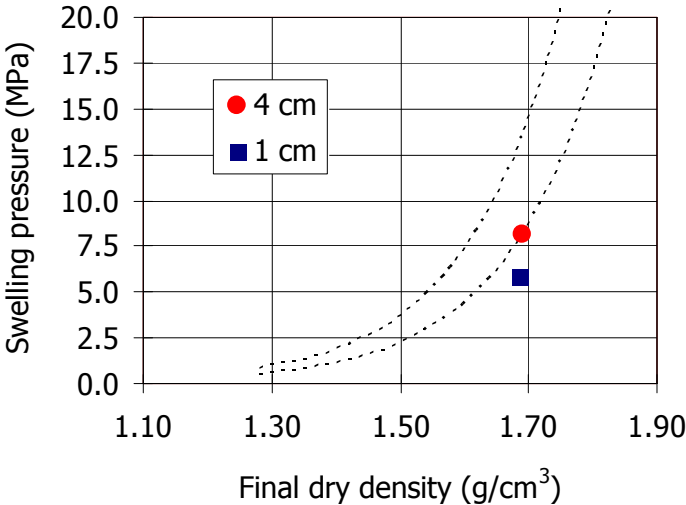
Figure 33.- Swelling pressure of samples from test HB4. The distance from the heater is indicated in the legend. The lines indicate the expected range of variation for untreated FEBEX bentonite

4.4. Aqueous extracts

Concentration of soluble elements was analyzed in the four sections represented in Figure 9 from aqueous extracts obtained by mixing dry bentonite and deionised water in a ratio 1:8 (S:L). To understand the distribution of elements along the column comparison with the results obtained from tests HB1 to HB3 is made.

Values obtained of the analysis of the soluble anions are displayed in Table XX and Figure 34. Cell HB4 (4.5 years) has a soluble chloride distribution similar to the cell HB3 (18 months). However, sulphate seems to achieve a maximum in an intermediate zone near the heater. Soluble salts migrating through the concrete plug concentrate as a function of time towards the heater zone and soluble cations also concentrate at this zone (Table XXI and Figure 35). However at HB4, soluble Na and Ca are less concentrated in the heater section than in the preceding section, in agreement with the corresponding sulphate maximum.

Table XX.- Soluble anions concentrations measured in the aqueous extracts (1:8 S/L) for tests HB1 to HB4.

	Section	mmol soluble anion / 100g dry bentonite	
		Cl^-	SO_4^{2-}
HB1	Hydration zone	0.013	0.016
	Intermediate zone	0.027	2.041
	Heating zone	6.124	0.886
HB2	Hydration zone	0.139	0.094
	Intermediate zone	0.047	0.121
	Heating zone	6.225	2.949
HB3	Interface	0.033	0.025
	Hydration zone	0.024	0.022
	Intermediate zone upper	0.021	0.027
	Intermediate zone lower	0.018	0.063
	Heating zone	9.266	2.173
HB4	Interface	0.042	0.054
	Hydration zone	0.010	0.004
	Intermediate zone upper	0.048	0.097
	Intermediate zone lower	0.423	3.012
	Heating zone	7.338	0.891
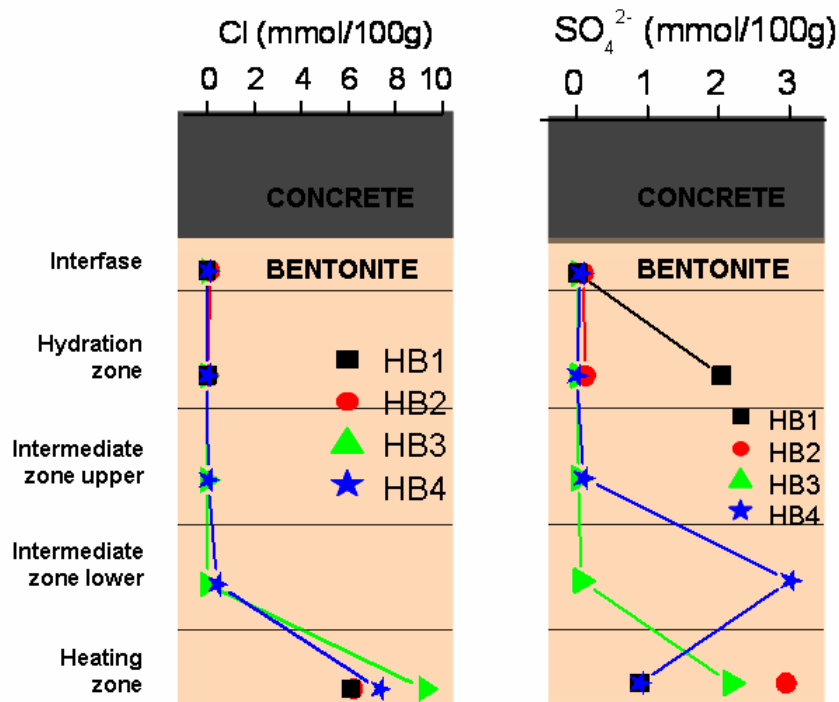
Figure 34.- Movement of chlorides along the bentonite block in cells HB1 to HB4 (aqueous extract solid:liquid 1:8).

Table XXI.- Soluble cations concentrations measured in the aqueous extracts (1:8 S/L) for tests HB1 to HB4.

Duration	Section	mmol soluble cation / 100g dry bentonite			
		Ca^{2+}	Mg^{2+}	Na^+	K^+
HB1	Hydration zone	0.08	0.00	2.37	0.03
	Intermediate zone	0.08	0.07	6.43	0.02
	Heating zone	0.26	0.38	7.51	0.05
HB2	Hydration zone	0.01	0.01	1.51	0.01
	Intermediate zone	0.01	0.00	1.63	0.02
	Heating zone	0.71	0.98	9.51	0.19
HB3	Interface	0.04	0.04	2.73	0.03
	Hydration zone	0.02	0.01	2.26	0.02
	Intermediate zone upper	0.01	0.03	1.60	0.01
	Intermediate zone lower	0.01	0.01	2.21	0.01
	Heating zone	0.78	0.98	10.75	0.25
HB4	Interface	0.03	0.02	2.80	0.03
	Hydration zone	0.03	0.01	2.26	0.02
	Intermediate zone upper	0.03	0.01	2.31	0.01
	Intermediate zone lower	0.26	0.16	6.94	0.12
	Heating zone	0.39	0.85	8.36	0.31
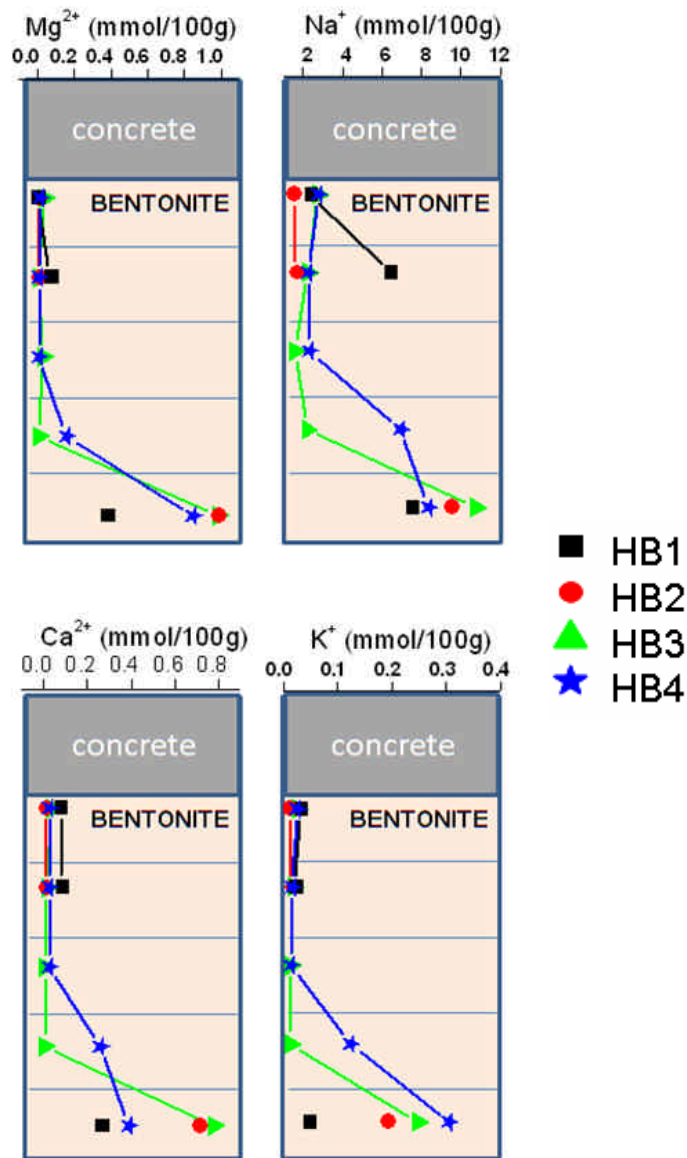
Figure 35.- Movement of cations along the bentonite block (aqueous extract solid:liquid 1:8).

4.5.   Exchangeable cations

Table XXII shows the values of the exchangeable cations measured along the bentonite blocks for the HB1 to HB4 tests. The evolution of exchangeable cations for the HB4 test is shown in Figure 36.

The behaviour of magnesium, sodium and calcium is affected both by exchange reactions and dissolution/precipitation processes, which depend also on the duration of the tests. The distribution of these exchangeable cations varies along the bentonite blocks.

The average value of calcium increases with time (from HB1 to HB4) and in the heating zone has the same values obtained for the unaltered FEBEX bentonite (35 meq/100g). Higher values at the hydration and intermediate zones are interpreted as due to the dissolution of calcite.

Table XXII.- Exchangeable cations (meq/100g) (CsNO3 0.5 N pH 7) measurements in the HB1 to HB4 dismantled cells.

Duration	Section	Ca^{2+}	Mg^{2+}	Na^+	K^+
HB1	Hydration zone	35	17	34	3
	Intermediate zone	37	25	26	3
	Heating zone	33	36	21	3
HB2	Hydration zone	42	13	35	3
	Intermediate zone upper	41	19	33	3
	Intermediate zone lower	44	15	31	3
	Heating zone	41	31	19	3
HB3	Interface	39	23	35	4
	Hydration zone	47	18	17	4
	Intermediate zone upper	44	18	36	4
	Intermediate zone lower	43	21	34	3
	Heating zone	37	50	20	5
HB4	Interface	52	9	38	2
	Hydration zone	46	6	44	2
	Intermediate zone upper	41	9	23	2
	Intermediate zone lower	51	28	20	2
	Heating zone	32	52	19	3
FEBEX bentonite		40	32	29	3
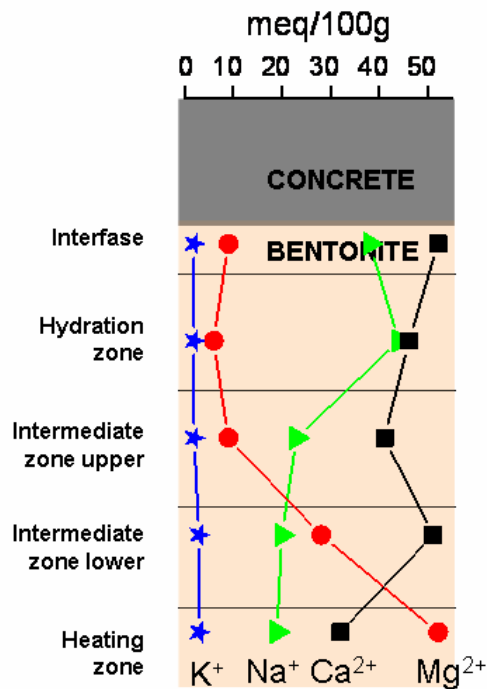
Magnesium and sodium seem to follow complementary trends along the bentonite column. Exchangeable sodium increases close to the hydration surface and drops near the heating zone, whereas magnesium decreases in saturated zones and increases near the heater. Sodium exchanges by magnesium in the saturated areas. Magnesium is released from the interlayers to pore water in the coolest zone and is transported to the hottest zone. Near the heater, magnesium released in saturated areas enters the exchange complex.

Cation exchange capacity of the small HB4 samples very close to the interface (Figure 9) is within the original bentonite values (Table XXIII). The procedure for the displacement of cations in these samples was adapted to use, duplicated, < 0.2 g of sample. The displacement was done with ammonium chloride (0.25 M at pH 7), three times, and the obtained solution, once diluted (at least 1:10) was measured by HPLC ion chromatography. The results agree with the general trend described above. Calcium and sodium dominate the exchange complex and have increased since 18 months (HB3) at the HB interface. In contrast, magnesium is complementary depleted, migrating towards the heater zone, although some precipitation of Mg rich phases at the alkaline interface cannot be discarded (Fernández et al., 2009).

Table XXIII.- Exhangeable cations distribution and cation exchange capacity expressed as the sum of the exchangeable cations at the concrete-bentonite interface. The values are refered as moles of charge in 110 ºC dry clay weight basis.

Sample	meq/100g				
	Na^+	K^+	Ca^{2+}	Mg^{2+}	**SUM**
HB4 02 --- 3-7 mm	42.2 ± 0.1	3.8 ± 0.1	62.5 ± 0.3	6.9 ± 0.5	115.5 ± 0.9
HB4 03 --- 7-11 mm	46.5 ± 1.2	3.7 ± 0.1	51.9 ± 0.8	6.2 ± 0.3	108.4 ± 2.3
HB4 04 --- 11-15 mm	45.8 ± 0.8	4.0 ± 0.1	66.3 ± 0.5	6.3 ± 0.1	122.5 ± 1.3

4.6.   Mineralogy at the concrete-bentonite interface

The concrete-bentonite interface was investigated by means of sampling and preparation procedures at different levels. Figure 37 shows the detail of the situation of two singular precipitates located, (1) at the hydration source in the upper concrete interface (a white powder) and (2) in discontinuous areas within the concrete-bentonite interface (whitish sheets or crusts). Concrete matrix was scrapped at several depths to obtain small quantities of sample, avoiding the sampling of coarse quartz aggregates, in order to study the effects of hydration in the concrete mineralogy. Besides, bentonite was divided in several millimetre sections near the interface for a detailed mineralogical study by means of XRD techniques. SEM-EDX studies were carried out in small fresh fractured specimens at the interface and by the registration of EDX chemical linear profiles through longitudinal polished sections going from the concrete plug to the first 15 mm of compacted bentonite.
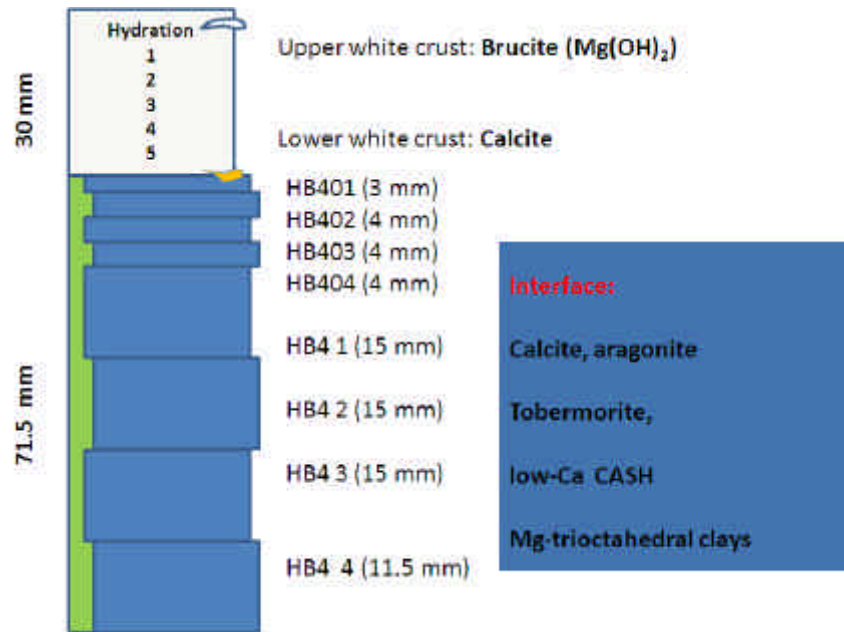
Figure 37.- Detailed notation of samples taken for the characterization of the HB4 cell.

4.6.1 FTIR data

FTIR spectra of the concrete (Figure 38), following the hydration path, show a generalized carbonation of the matrix indicated by the presence of calcite bands (1448 cm^{-1} and 811 cm^{-1}). Brucite and CSH-gel bands were also identified. At the bentonite interface, bentonite characteristic bands are identified at 1641, 1476 and 1033 cm^{-1}, but changes in Al-Mg-Fe bands 1000 a 700 cm^{-1} suggest the presence of new formed or modified clay minerals.

(a)   (b)
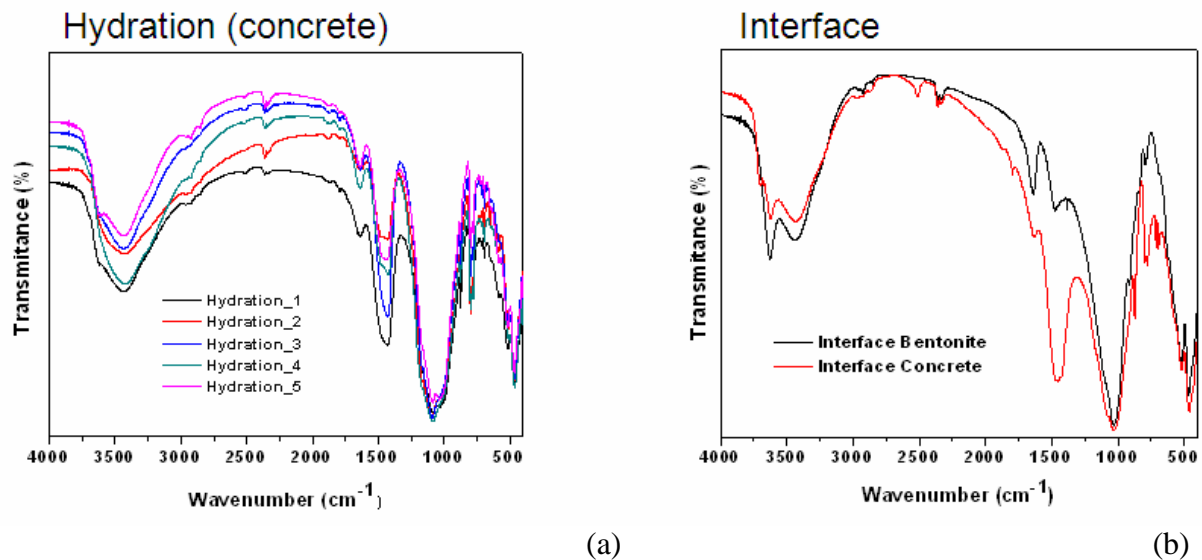
Figure 38.- FTIR spectra for the concrete (a) and concrete-bentonite interface (b)

4.6.2 XRD data

Materials analyzed by XRD come from very small samples of < 0.1g scrapped in the concrete cement matrix (CEM1 to 8 in Table XXIV). They were grinded in an agate mortar and mounted on a zero background silicon wafer. The white powder at the hydration source is composed of brucite and aragonite which indicated that carbonates and magnesium precipitated at the hydration-concrete interface and, consequently these components have been "filtered" by the concrete disc. Calcite is always identified in all of the cement matrix samples and some ettringite is identified in one sample. Calcite and aragonite have precipitated also at the concrete/bentonite interface, together with the identification of new sharp reflections that in a preliminary determination have been assigned to a low Ca/Si anorthite-like phase (CASH-like phase), which should be further studied. The remaining bentonite samples displayed more or less the typical FEBEX bentonite XRD pattern. The XRD patterns are presented in Figure 39 and the detail for the cement matrix (CEM2) and the interface whitish crusts (C-powder) in Figure 40 and Figure 41, respectively.

The calcite peak in the cement matrix seems to decrease from the bentonite interface to the hydration side. This suggests a selective leaching of the cement paste in areas close to the hydration, which was anticipated by FTIR data. Figure 42 shows differences in calcite peak intensity from hydration (CEM1) to the bentonite interface (CEM8). These samples have been selected to plot because they have similar quartz peak intensities, so that calcite peak intensities can be compared.

In order to confirm the presence of CSH-like tobermorite phases, usually identified by a broad peak at 11 Å, the region of low XRD angles (2-15 ^{0}2?) has been deconvolved with the software DRXWIN (V. Primo ©). Table XXV lists the positions and the weight of their contributions (integrated area in arbitrary units) considering the presence of three peaks, which normally produced a good fitting of the XRD profile (Figure 43 and Figure 44). The bentonites near the interface have well developed peaks at near 12 Å (Na form of montmorillonite) and 10 Å (dehydrated montmorillonite), which is in agreement with the sodium enrichment of the exchange complex. The presence of CSH phases could not be identified because their XRD peaks can be overlapped to effects close to 10-12Å peak region. In contrast, the bentonite near the heater, HB4 4 shows virtually a unique reflection peak at 14.4 Å related to the predominance of Ca-Mg forms of montmorillonite (Figure 44).

Table XXIV.- Mineralogical composition of materials studied in HB4 concrete –bentonite cell

Sample	Qtz	Cal	Pl	Kfs	Etringite	"CASH"	Mmt	"Mica"	Arg	Brc	Crst	Other Å
hydration									X	XXX		3.04 + 2.73
CEM1	XXX	X	X	X	-		-	Dt			X	
CEM2	XX	X	X	X	X		-	Dt			X	
CEM3	XXX	X	X	X	-			Dt			X	
CEM4	XX	X	X	X	-		-				X	
CEM5	XX	X	X	X	-		-				X	
CEM6	XX	X	X	X	-		-				X	6.46
CEM7	XX	X	X	X	-						X	
CEM8	XX	XXX	X	X	-		-				X	
C-powder	X	X				X	X		X		X	
HB4 01	-	-	X			?	X	Dt			X	3.74
HB4 02	-	-	X			?	X	Dt			X	3.74
HB4 03	-	-	X			?	X	Dt			X	3.74
HB4 04	-	-	X				X	Dt			X	
HB4 1	X	-		X			XX				X	2.71
HB4 2	X	-	X				XXX				X	
HB4 3	X	-	X	X			XXX				X	
HB4 4	X	-					XXX				X	

Tr: possible. -: not detected, ?: posible but with overlapping to other plagioclase peaks. Brc: brucite, Arg: aragonite; Qtz: quartz, Cal: calcite, Pl: plagioclase, Kfs: K-feldspar, Mnt: montmorillonie, Crs: cristobalite. Dt: detected; X: significant (< 5 %); XX: abundant (5 – 10 %); XXX: major (> 80 %).
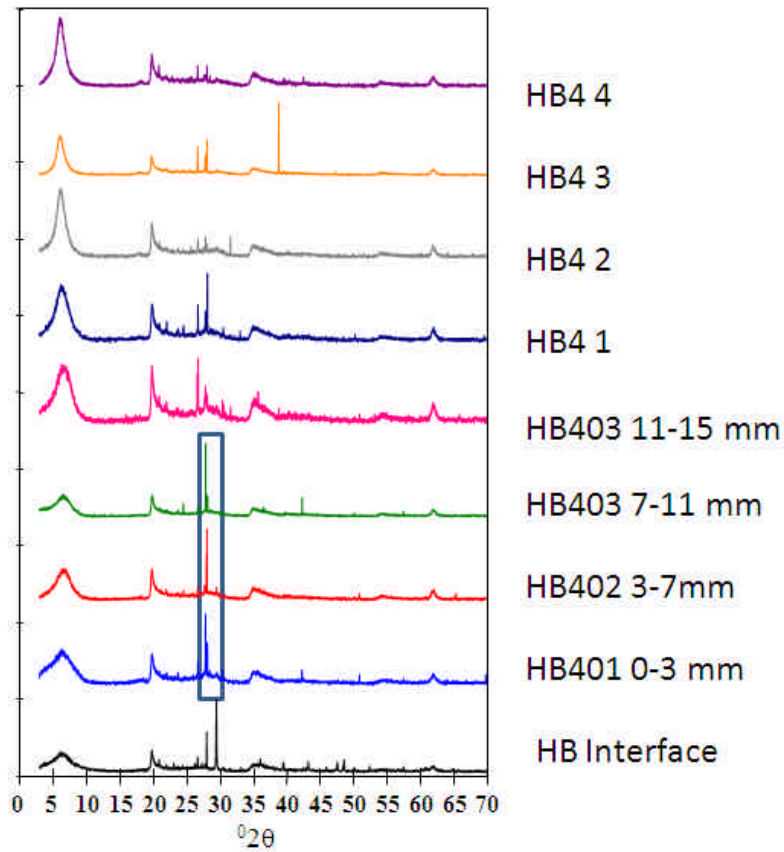
Figure 39.- XRD random powder patterns from the concrete/bentonite interface and the samples of compacted bentonite from the interface to the heater (HB41-HB4-4). Rectangular window show the significant development of plagioclase peaks.
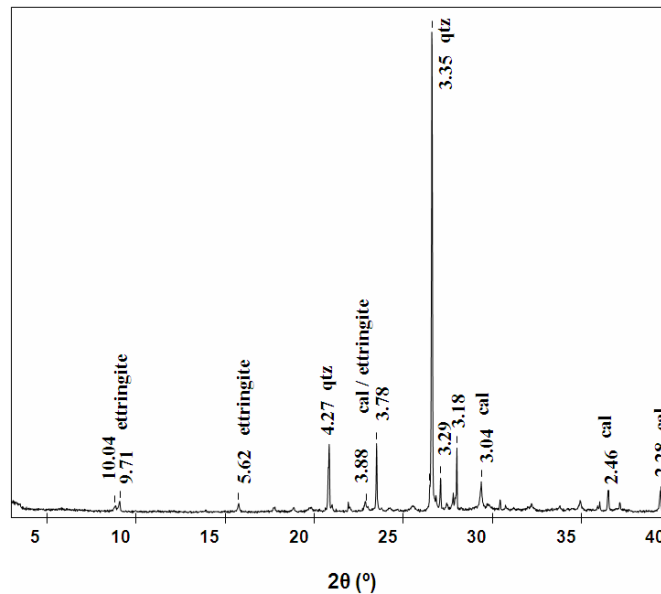
Figure 40.- Detail of the XRD diffraction pattern of the cement matrix CEM2. Qtz: quartz, cal: calcite. 10.04 Å is a mica component included with the mortar sand.
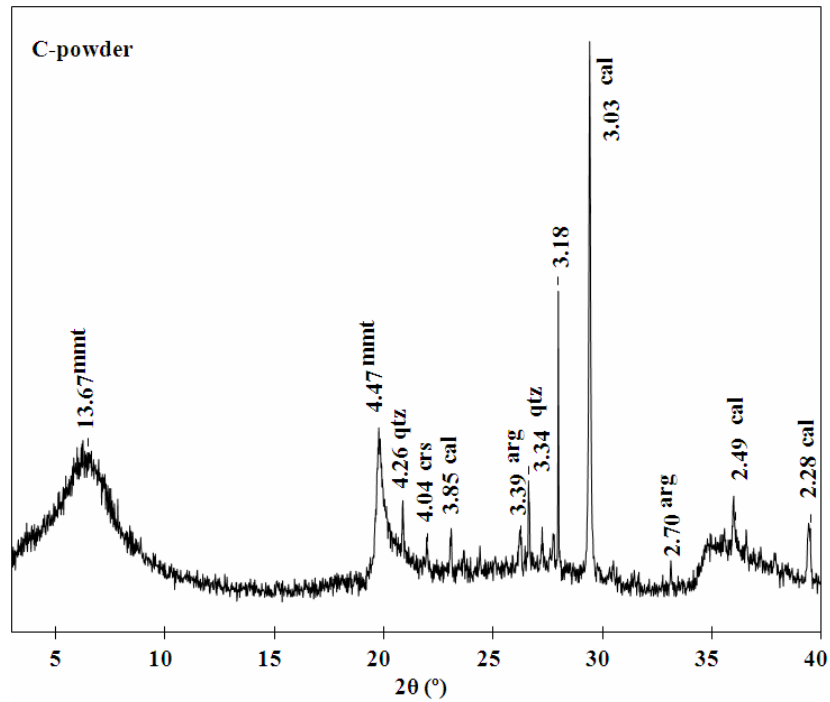
Figure 41.- Detail of the XRD random powder pattern of the whitish crust (C-powder) taken at the HB interface. mmt: montmorillonite, qtz: quartz, crs: cristobalite (overlapped with plagioclase peaks), arg: aragonite, cal: calcite. 3.18 Å sharp peak has not been assigned (see text.)
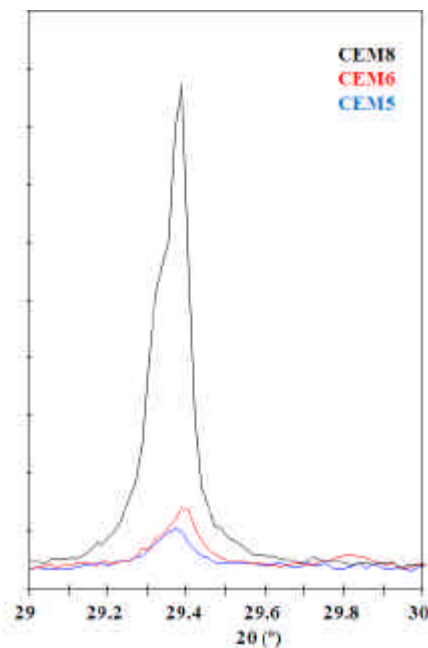
Figure 42.- Detail of the XRD random powder patterns showing the calcite peak of different cement matrices along the hydration to concrete-bentonite interface.The whitish crust (C-powder) was taken at the HB interface.

Table XXV.- Positions of the low angle XRD deconvolved peaks (see the example in Figure 43). Numbers on the right of the peak positions are integrated areas of the peaks in arbitrary units.

Sample	~ 14.5 Å	~ 12 Å	~ 10 Å
HB4 M01	14.44-972.39	11.76-273.96	10.16-301.91
HB4 M02	14.00-850.06	12.24-240.89	10.68-332.9
HB4 M03	13.93-882.26	11.78-182.08	10.27-147.5
HB4 M04	13.83-850.9	11.77-311.88	10.24-80.72
HB4 1	14.22-1540.36	11.98-557.09	10.15-25.07
HB4 2	14.44-2017.96	12.47-316.92	10.42-3.84
HB4 3	14.68-941.64	13.11-714.39	
HB4 4	14.40-2278.03	12.69-9.59	
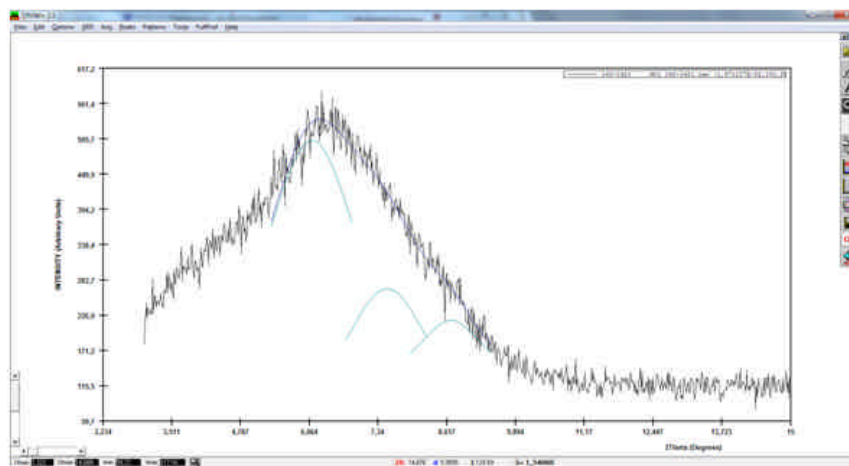
Figure 43.-. Deconvolution of the XRD pattern regarding the sample HB4 0; peaks at 14.4, 11.8 and 10.2 Å in a continuum broad band.
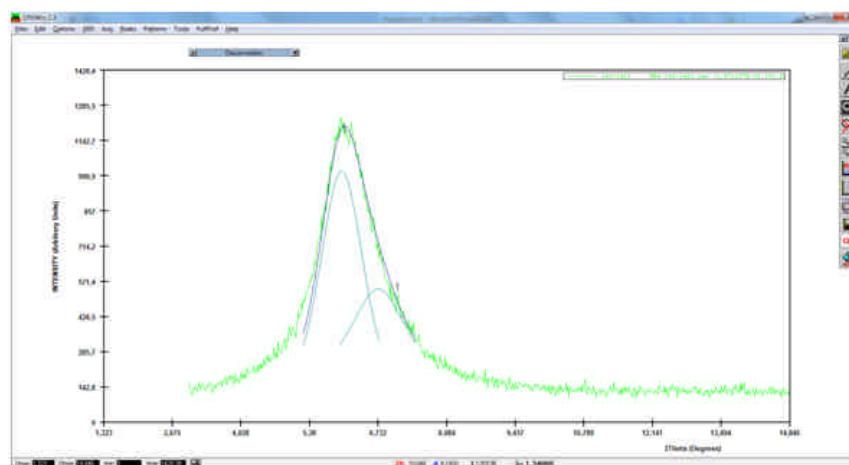
Figure 44.- Deconvolution of the XRD pattern regarding the sample HB4 4; peaks at 14.4 (major and symmetric band) and 12.7 Å low intensity band.

Oriented clay films (< 2 µm size fraction) have been prepared to separate and determine the nature of the different sheet silicates at the HB interface. Figure 45 compares the diffraction effects of the clay under air dried (ambient laboratory) conditions, solvated with ethylene-glycol (EG) vapour and heated to 550 ºC. The < 2 µm size fraction was previously homoionised in Mg exchangeable cation. Then, air dried Mg-montmorillonite basal spacing was 14.4 Å, when solvated in EG, the basal spacing of the mineral swells to 16.7 Å; and when heated to 550ºC, collapses to 9.6 Å. This is the standard behaviour of smectites indicative of non significant alteration of the montmorillonite in the first 3 mm of HB interface. Moreover, 11Å bands were not identified and the presence of tobermorite was not confirmed. There exists the possibility of having dissolved this mineral during the separation of the clay fraction (repeated sonication and suspension of clay in distilled water) and homionization procedure. This procedure involves the repeated treatment of the sample with $MgCl_2$ 0.5 M neutral solutions followed by 4-5 ethanol washings. Under these conditions CSH mineral, produced in alkaline medium, should be altered. As a consequence, a method of determination of CSH by means of separation procedures needs to be designed, avoiding homoionisation and using merely EG solvation to separate diffraction effects.
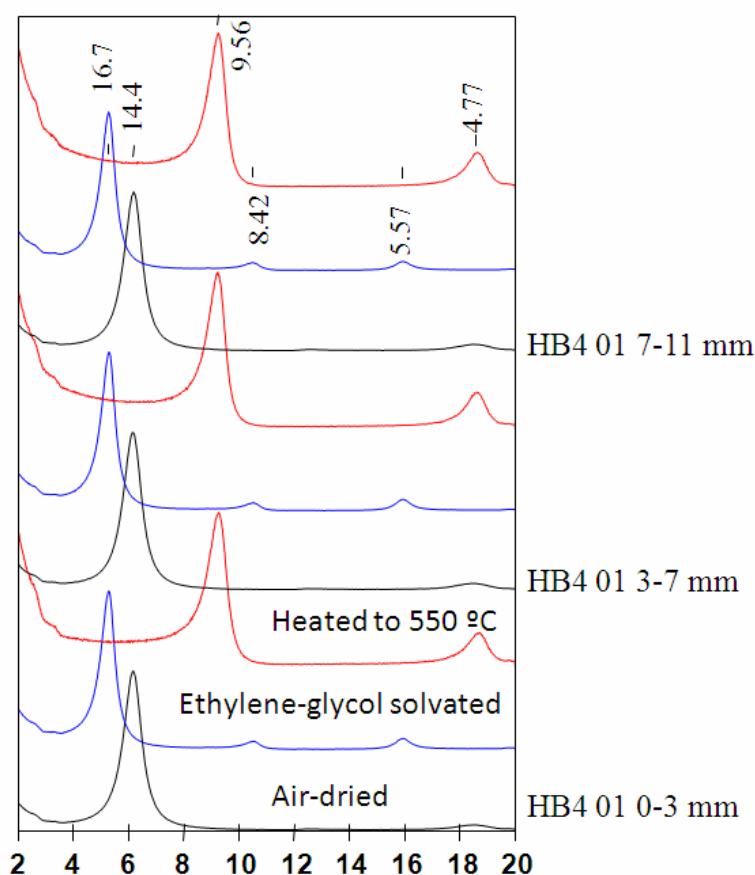
Figure 45.- Clay oriented films XRD patterns of samples in the HB interface. Numbers are the peak positions in Å

FTIR spectra have shown the modification of standard bentonite bands at the HB interface. The spacing 060 of sheet silicates (XRD angle region 59-63 Å; Figure 46) can indicate modifications in the nature of the octahedral layer of clay minerals. Montmorillonite shows a broad peak at 1.498 Å (di-octahedral Al^{3+} sheet silicate structure). This peak is

present in all samples, but the clay within the whitish crusts sampled at the HB interface showed peaks in the range of (060) tri-octahedral clays (1.53-1.52 Å) (full Mg^{2+}, Fe^{2+} occupation of octahedral positions in the sheet silicate structure). In the 0-3 mm interface sample (HB4 01), a peak shoulder can be observed in the 1.53-1.52 Å. These data confirm the possibility of formation of new tri-octahedral clays in small quantities, which should be further confirmed in the long–term experiments and with more SEM or TEM studies.
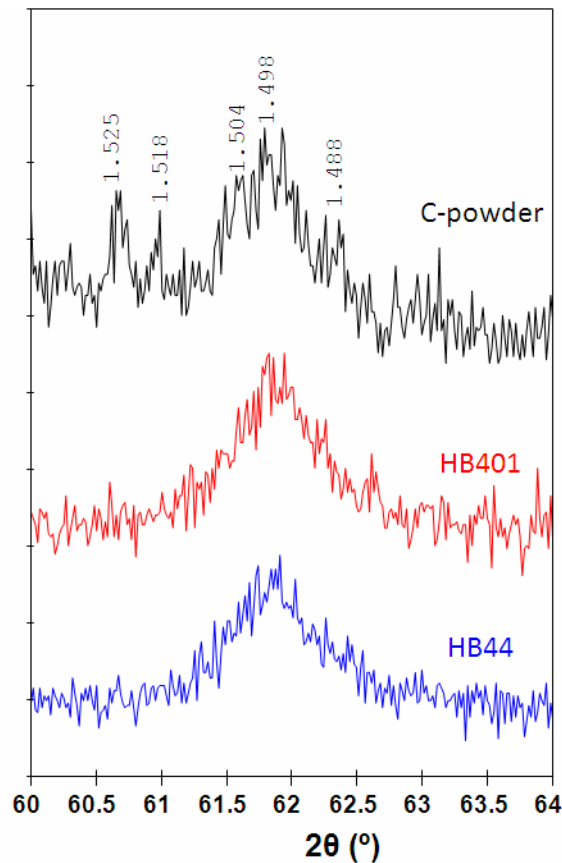
Figure 46.- 60-64 ^{0}2? XRD powder diffraction pattern showing the (060) spacing reflections for clay minerals.

4.6.3 SEM data

From the experiment HB4 dismantled on December 2010, after 4 years and 5 months of operation, a 10-mm thick slice was cut perpendicular to the concrete-bentonite interface, getting a sample 45-mm long (30 mm of concrete plus 15 mm of bentonite) by 10-mm wide for the study by electronic and optical microscopy (the optical analysis has not been performed yet).

During the dismantling of the column, the whole sample was rapidly wrapped by a textile adhesive tissue and then covered with a non-permeable elastic adhesive band to avoid contact with atmospheric conditions. Two 10 mm separated parallel vertical cuts 20 mm deep were rapidly done with a water refrigerated diamond disc from the concrete side without entering in the first 10 mm near the bentonite. The other 25 mm cut was performed with a stainless steel-diamond wire saw (Well2000™) without any cutting fluid entering near the concrete-bentonite interface. Each cut takes 7-10 days to be completed.

The concrete-bentonite sample was freeze-dried. The process consists of immersing the sample in liquid nitrogen (for 1 h) and, then, reduce the pressure (10^{-1} - 10^{-2} Pa at 20 °C for 3 days) to sublimate the frozen pore water directly from the solid phase to gas phase. After this process, the sample was kept under vacuum and embedded in low viscosity resin LR-White ®, which covers the pore space and harden the sample. The hardening process is a modification of the method described by Kim *et al.* (1995). Finally, the sample was polished (Figure 47) for analysis with an INSPECT FEI Scanning Electron Microscope (SEM).
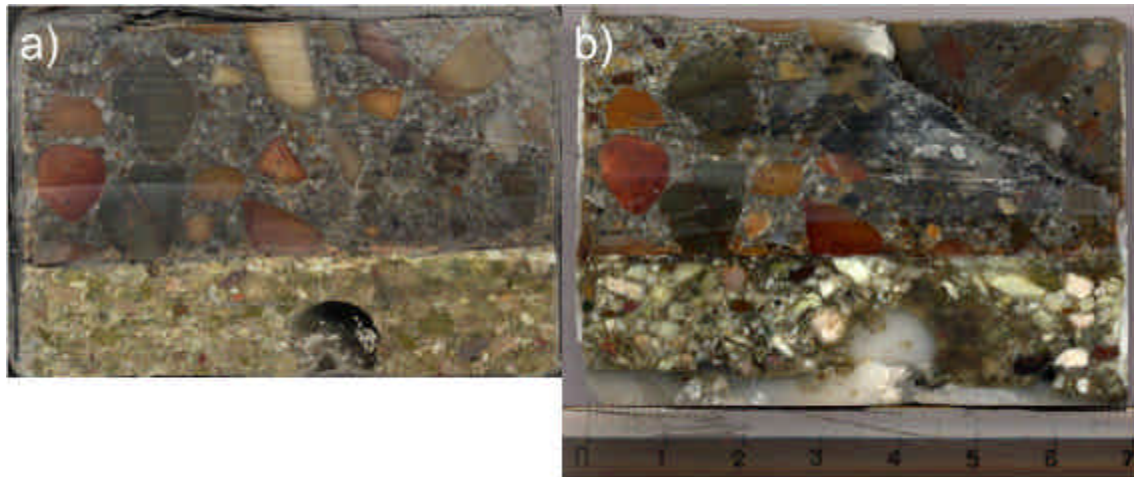

Figure 47.- a) photograph of the concrete-bentonite sample after the stainless steel-diamond wire cut, and b) after the resin embedment. The circular hole (covered by the white resin in photograph b) corresponds to the gap left by a temperature and RH sensor. Ruler units are in cm.

Some photographs were taken at the interface at different magnification ranges and specific analyses were performed with the EDX analyser. Two types of EDX mapping at low magnification (xy window size: 2.6 × 2.98 mm; x = along the interface direction, y = along the concrete-bentonite direction; 20 s/analysis at 25 kV) allowed the graphic representation of spatial distribution of elements (given as concentration of oxides):

- A map in the vertical direction of the concrete-bentonite column (i.e. perpendicular to the interface) – 48 analyses: a xy matrix 3×16.
- A map in bentonite, parallel to the interface – 56 analyses: a xy matrix 10×6 with some vacancies in the left side corner.

Quantitative elemental chemistry contour maps were represented with the data analysis and graphing software ORIGIN, version 8.

In addition, high magnification EDX analyses (xy window size: 297.53 × 256.15 µm) were performed in the vertical direction, perpendicular to the interface, with the objective to accurately detect diffusion processes at the interface. Only two parallel profiles were performed at high magnification (283 analyses: a xy matrix 2×147 with some not performed analyses in windows covered by 100% quartz grains in the concrete domain), therefore, the graphic representation was linear.

A detailed observation of the interface in the backscattering electron mode reveals the existence of desiccation cracks at microscale and a sub-millimetric gap presumable developed by an instant drying interface separation during the dismantling. In any case, a 1 mm portion

of the bentonite interface is crossed by sub-parallel whitish veinlets, characteristic of calcium enrichments (Figure 48). A fresh fractured chip of these bentonite interface rims was observed in secondary electrons mode and analysed. Calcite, mainly in the bentonite, and calcium silicates (aluminates) hydrates (C–A–S–H) type materials were identified (Figure 49; Table XXVI). However, these later phases must be confirmed by additional spectroscopic techniques like TEM.
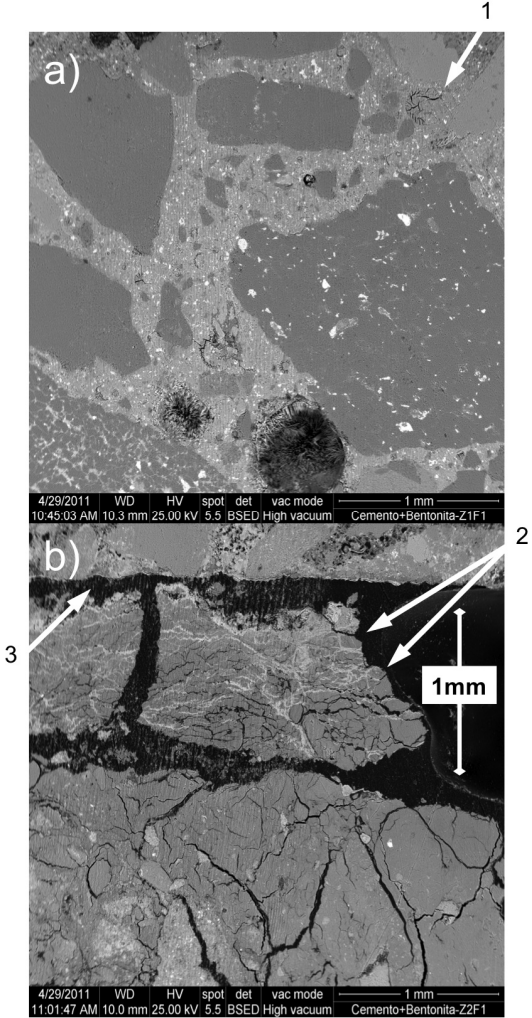

Figure 48.- SEM photographs a) in the concrete domain, b) at the concrete-bentonite interface. 1: desiccation cracks at microscale; 2: sub-parallel whitish veinlets and 3: sub-millimetric gap presumable developed by an instant drying interface separation during the dismantling.
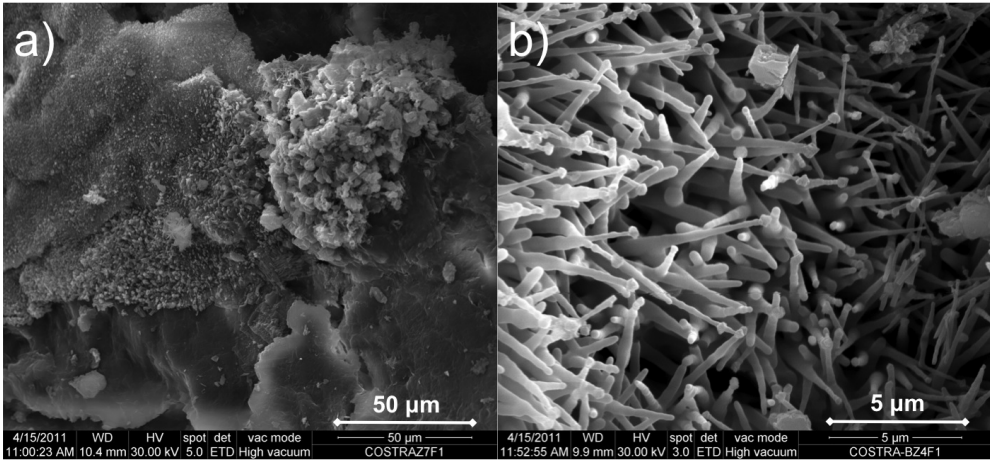

Figure 49.- SEM pictures at the interface a) new-formed calcite crystals, b) CASH-type phases.

Table XXVI.- Chemical composition of EDX analyses performed on selected sites of Figure 49 a) and b).

Composition in oxides	Bentonite crust (Fig. 2a; in wt.%)	Cement face rods (Fig. 2b; in wt.%)
MgO	-	-
Al_2O_3	2.68	3.63
SiO_2	10.19	65.84
CaO	87.13	29.22
Na_2O	-	1.31

From the low magnification maps in the vertical direction of the concrete-bentonite column (Figure 50 and Figure 51), it can be outlined an irregular Mg increase and Al depletion in the first millimetres of interface. The calcium front has exceeded the first two mm of interface confirming the alkaline diffusion. The distribution of Si and Na is very heterogeneous and not any diffusion trend can be derived from the results. S and Al show a gradient of concentration in the interface related with the different composition in both materials.

Some punctual hotspots of Fe, K and Ti are observed in the concrete. However, these elements (shown in oxides) may exhibit low concentration in both materials, concrete and bentonite, and not any diffusion trend can be derived from the mapping.

The low magnification maps in bentonite (along sequential profiles parallel to the concrete-bentonite interface) show much heterogeneity related to the minerals in bentonite (Figure 52). However, due to the low magnification analyses, it cannot be inferred a diffusion plume from concrete. A high concentration spot in TiO_2 is observed near the interface. The diffusion plume of this TiO_2 hotspot is radially detected up to 3 mm, and coincides with a decrease in Fe_2O_3 in the same region. Presumably, this could be due to a Ti-bearing accessory mineral in bentonite such as rutile, located in this region (Fernández *et al*., 2004; Fernández and Villar, 2010). An increase in MgO is observed at the bottom end of the map (15 mm from the interface). This is somehow unexpected, but due to the low magnification of the analyses (large analysis windows size) that limit the quantification resolution, and the lack of data below 15.6 mm, the interpretation of this MgO enrichment is not possible. In fact, exchangeable magnesium is depleted in this zone, but small quantities of Mg tri-octahedral clays are presumed to be formed at the interface.

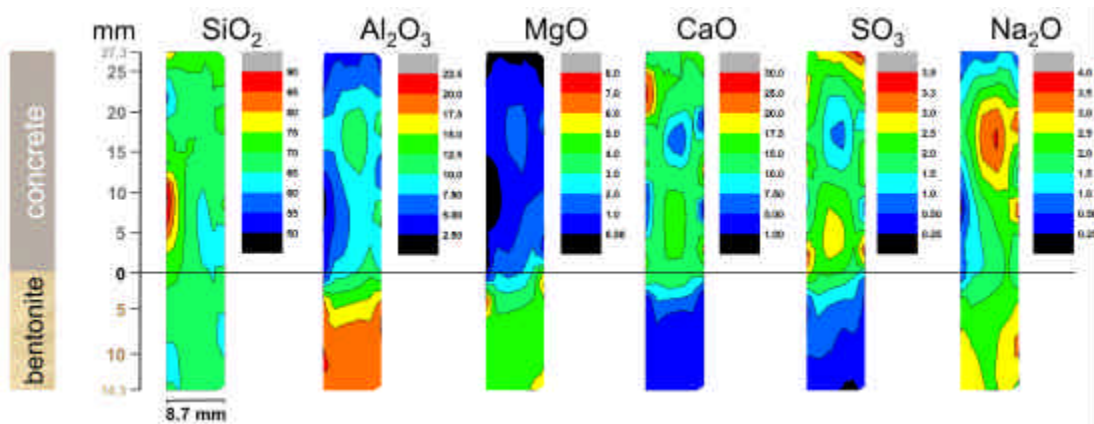*Figure 50.- Low magnification EDX mapping along the concrete-bentonite direction for Si, Al, Mg, Ca, S and Na oxides.*
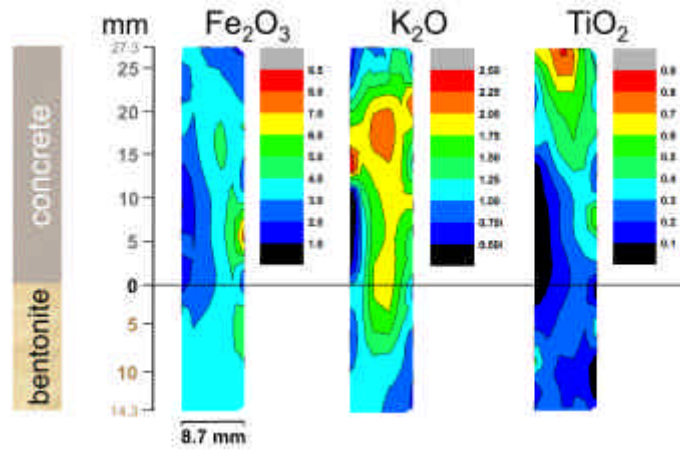
Figure 51.- Low magnification EDX mapping along the concrete-bentonite direction for Fe, K and Ti oxides.
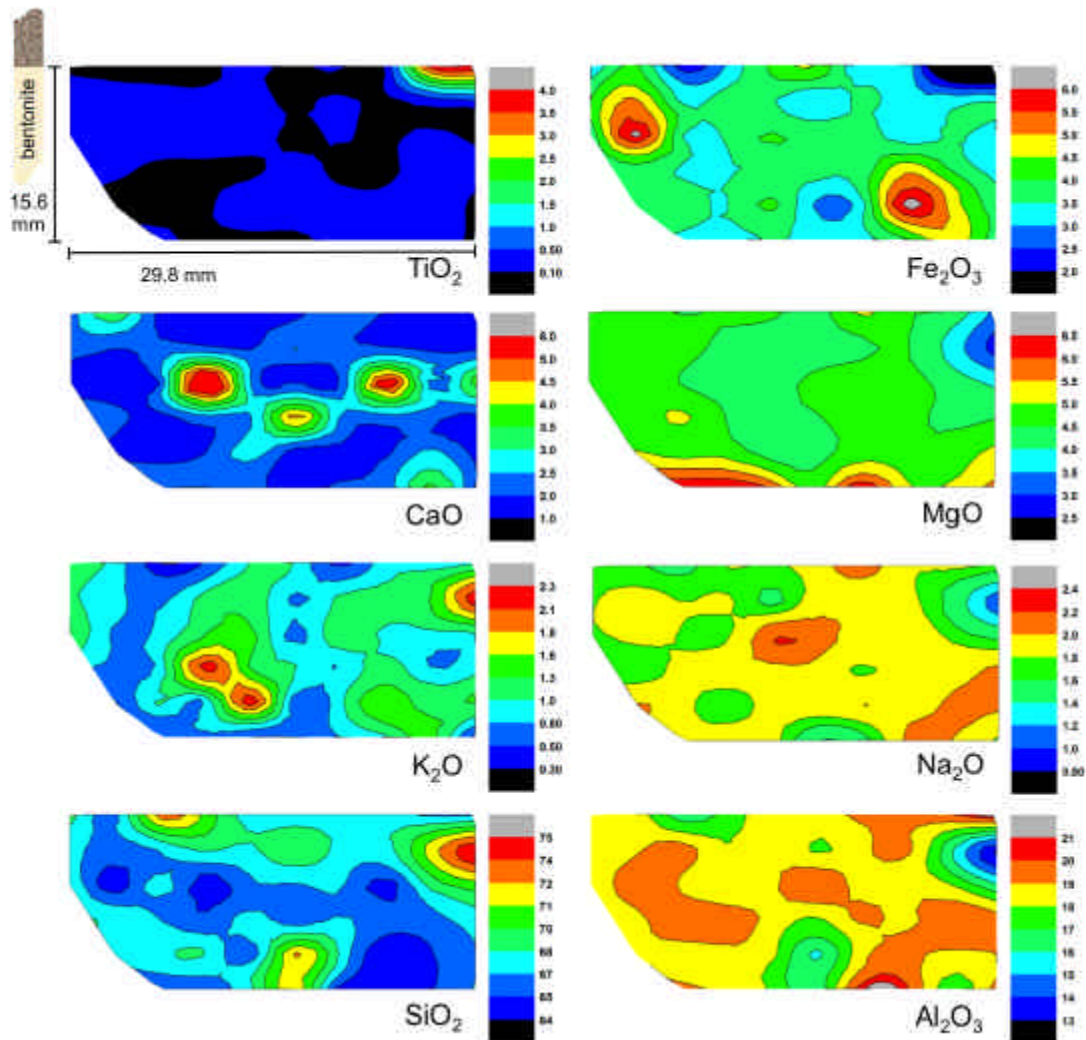
Figure 52.- Low magnification EDX mapping in bentonite, parallel to the interface. The left bottom corner, not analysed, corresponds to the gap caused by the T–RH sensor.

In order to improve the interpretation of the diffusion fronts, high magnification EDX analyses were performed on the same concrete-bentonite sample. Each major element (in oxide composition) has been represented independently (Figure 53). The content in SiO_2 and CaO is dominant in concrete. Several grains of quartz can be derived along the concrete profile (SiO_2 content near 100%). Along the profile analysed by EDX, one of these grains of quartz is present in concrete very near the interface with bentonite, hindering the diffusion plume of other elements (i.e. negligible alkaline diffusion plume is expected if a grain of quartz is blocking the diffusion path, this could be more visible when the cement matrix is at the interface). Despite this, the calcium and magnesium profiles clearly show enrichment in the first 1–1.5 millimetre of bentonite from the interface, as a result of the net effect of the alkaline diffusion at the interface.

Figure 53.- High magnification EDX profiles along the concrete-bentonite column, perpendicular to the interface.

5. Future work and considerations for the next dismantling

Tasks to be developed on the dismantling of the ~ 7 years medium FB and HB cells:

- Porosity should be measured in samples near the HB interface.

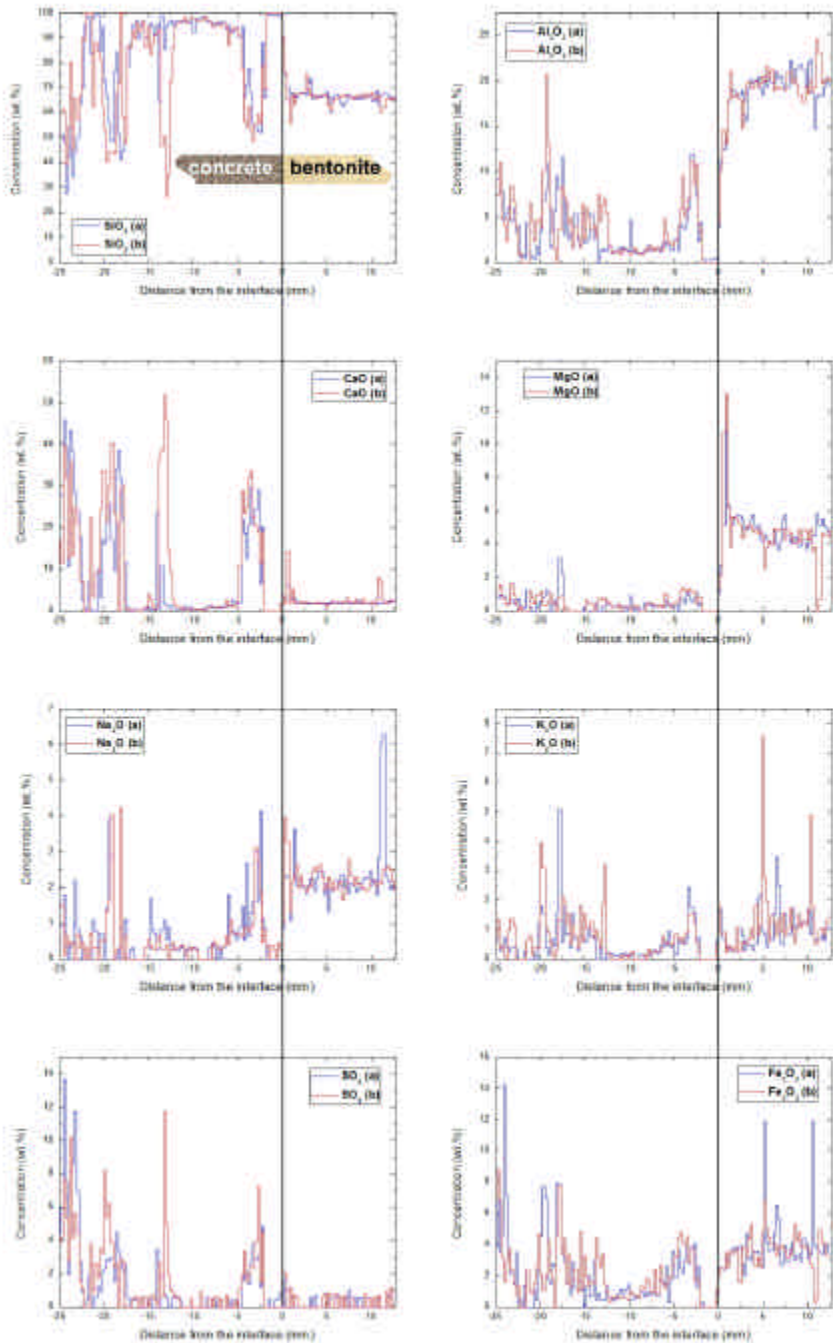- Care should be taken to maintain water pressure at the injection ports in order to check the impact of the discontinuous hydration during the first three years in the results obtained at ~4 and ~7 years

- To measure carefully the final water content of the HB cells components: concrete probe and bentonite, in order to confirm that actual water content is higher than in the FB cells caused by the intrusion of water through gaps or other voids than bentonite porosity.

- It would be necessary in the longest term experiments to measure both porosity and swelling pressure in a section from the concrete/bentonite interface.

- More EDS mappings are necessary to characterize the bentonite/iron or concrete interface. Preparations for optical observation will be available soon.

- More characterization work: selective extraction, TEM will be needed to identify conclusively which CSH or CASH phases are present at the concrete-bentonite interface. 11 Å bands were not identified during the XRD clay mineral identification, and the presence of tobermorite was not confirmed. The same is necessary for iron/bentonite interface and to identify precisely iron corrosion products.

- Concrete matrix has been significantly substituted by calcite (carbonation) and slightly leached at the hydration interface. Mg in the porewater precipitates as brucite in the hydration/concrete interface, and aragonite forms, either at the hydration interface or in the HB interface. The formation of aragonite is related to carbonate precipitation under saline conditions.

- FTIR and XRD data confirm the possibility of formation of new tri-octahedral clays in small quantities, which should be further confirmed in the long–term experiments and with more SEM or TEM studies. SEM-EDX profiles at the highest resolution have confirmed the calcium and magnesium enrichment in the first 1–1.5 millimetre of bentonite from the concrete interface. The Mg behaviour is complex and difficult to characterize as it became depleted in the exchange complex and by contrast, presumably precipitated as silicate at the concrete interface. Some studies at high resolution scale should be conducted in order to determine the extension of Mg-silicate phase formation.

6. REFERENCES

Campos, R., González, A.M., Barrios, I. (2011ª): Experimento interacción bentonita-hierro: análisis de la porosidad y superficie específica – Celda 3. Informe Técnico CIEMAT/DMA/2G210/4/11. Madrid, 10 pp.

Campos, R., González, A.M., Barrios, I. (2011b): Ensayo de interacción bentonita/hormigón: análisis de la porosidad y superficie específica – Muestras HB1-HB4. Informe Técnico CIEMAT/DMA/2G210/1/11. Madrid, 13 pp.

Cuevas, J., Villar, M.V., Fernández, A.M., Gómez, P., Martín, P.L. (1997): Pore waters extracted from compacted bentonite subjected to simultaneous heating and hydration. Applied Geochemistry 12: 473-481.

Cuevas, J., Villar, M.V., Martín, M., Cobeña, J.C., Leguey S. (2002): Thermo-hydraulic gradients on bentonite: distribution of soluble salts, microstructure and modification of the hydraulic and mechanical behaviour. Applied Clay Science 22: 25-38.

Cuevas, J. (2005): Geochemical recations in FEBEX bentonite. In: ANDRA (ed.): Ecoclay II: Effects of Cement on Clay Barrier Performance – Phase II. Final Report. EC project nº FIKW-CT-2000-00028; Andra Report nº CRPASCM04-0009, 381 pp.

Cuevas, J., Vigil de la Villa, R., Ramírez, S., Sánchez, L., Fernández, R., Leguey S. (2006): The alkaline reaction of FEBEX bentonite: a contribution to the study of the performance of bentonite/concrete engineered barrier systems. Journal of Iberian Geology 32 (2): 151-174.

Drever J.I. (1988): The Geochemistry of Natural Waters. Prentice Hall, New Jersey.

ENRESA (2000): FEBEX Project. Full-scale engineered barriers experiment for a deep geological repository for high level radioactive waste in crystalline host rock. Final Report. Publicación Técnica ENRESA 1/2000, Madrid, 354 pp.

ENRESA (2006): FEBEX Full-scale Engineered Barriers Experiment, Updated Final Report 1994-2004. Publicación Técnica ENRESA 05-0/2006, Madrid, 590 pp.

ENRESA (2008): Chemical (thermo-hydromechanical) evolution of the EBS: evolution of porewater chemistry; effects of canister corrosion and concrete degradation; and radionuclide retention. NF-PRO project. Enresa, Documentos internos de referencia 03/2008.

Escribano, A., Torres, E., Turrero, M.J., Martín, P.L., Gómez P. (2008): Concrete degradation and its influence on the geochemical conditions at the concrete/ bentonite interface under repository conditions. Euradwaste'08. Seventh European Commission Conference on the Management and Disposal of Radioactive Waste. Community Policy and Research &Training Activities. Euratom EUR 24040. ISBN: 978-92-79-13105-g. Editor: C. Davies.

Fernández, A.M., Baeyens, B., Bradbury, M., Rivas P. (2004): Analysis of the porewater chemical composition of a Spansh compacted bentonite used in an engineered barrier. Physics and Chemistry of the Earth 29: 105-118.

Fernández, R., Mäder, U.K., Rodríguez, M., Vigil de la Villa, R., Cuevas, J. (2009): Alteration of compacted bentonite by diffusion of highly alkaline solutions. European Journal of Mineralogy 21: 725-735.

Fernández, A.M., Villar M.V. (2010): Geochemical behaviour of a bentonite barrier in the laboratory after up to 8 years of heating and hydration. Applied Geochemistry 25: 809-824.

Hidalgo, A., Alonso, C., Andrade, C., Fernández, L. (2003): Review of concrete formulations defined for nuclear waste repositories. ECOCLAY II, WP 2, IETCC (CSIC).

Huertas, F. Farias, J., Griffault, L., Leguey, S., Cuevas, J., Ramírez, S., Vigil de la Villa, R., Cobeña, J., Andrade, C., Alonso, M.C., Hidalgo, A., Parneix, J.C., Rassineux, F., Bouchet., Meunier, A., Decarreau, A., Petit, S., Vieillard, P. (2000): Effects of cement on clay barrier performance ECOCLAY I project. EUR 19609 final report.

Idemitsu, K., Furuya, H., Inagaki Y. (1993): Diffusion of corrosion products of iron in compacted bentonite, edited by C.G. Interranteand R.T. Pabalan, (Mater. Res. Soc. Symp Proc. 294, Sci Basis XVI, 1993) pp 467-470.

Kamei, G., Oda, S., Mitsui, S., Shibata, M. Shinozaki, T. (1999): Fe(II)–Na ion exchange at interlayers of smectite: adsorption–desorption experiments and a natural analogue. Engineering Geology 54 (1): 15.

Kim, J., Peacor, D. R., Tessier, D., and Elsass, F., 1995. A technique for maintaining texture and permanent expansion of smectite interlayer for TEM observations. Clays and Clay Minerals 43: 51-57.

Leguey, S., Cuevas, J., Martín, M., Vigil de la Villa, R., Ramírez, S., García R. (2002): Procesos geoquímicos y modificaciones texturales en bentonita FEBEX compactada sometida a un gradiente termohidráulico. Publicación técnica 10-02, ENRESA, Madrid.

Martín, M., Cuevas, J., Leguey S. (2000): Diffusion of soluble salts under a temperature gradient after the hydration of compacted bentonite. Applied Clay Science 17(1-2): 55-70.

Moore, D.M., Reynolds, R.C., Jr. (1989): X-Ray Diffraction and the Identification and Analysis of Clay Minerals: Oxford (Oxford Univ. Press).

Sánchez, M., 2004. Thermo-hydro-mechanical coupled analysis in low permeability media. PhD Thesis. Universitat Politècnica de Catalunya (UPC), Barcelona, 281 pp.

Smart, N.R., Blackwood, D.J., Werme L. (2002): Anaerobic Corrosion of Carbon Steeland Cast Iron in Artificial Groundwaters: Part 1 - Electrochemical Aspects, Corrosion 58: 547-559.

Taniguchi, N., Kawasaki, S., Kawakami, N., Kubota, M. (2004): Corrosion behaviour of carbon steel in contact with bentonite under anaerobic conditions Proceedings of the 2nd Internacional Workshop Eurocorr, edited by NAGRA (2004), pp 24-34.

Torres, E. Escribano, A., Baldonedo, J.L., Turrero, M.J., Martín, P.L., Peña, J., Villar M.V. (2009): Evolution of the geochemical conditions in the bentonite barrier and its influence on the corrosion of the carbon steel canister. In: Scientific Basis for Nuclear Waste Management XXXII, edited by Neil C. Hyatt, David A. Pickett, Raul B. Rebak. Mater. Res. Soc. Symp. Proc. Volume 1124: 301-306. ISBN: 978-1-60511-096-7.

Torres, E., Escribano, A., Turrero, M.J., Martín P.L. (2009): Temporal evolution of the concrete-bentonite system under repository conditions. En: Scientific Basis for Nuclear Waste Management XXXII, edited by Neil C. Hyatt, David A. Pickett, Raul B. Rebak. Mater. Res. Soc. Symp. Proc. Volume 1124: 295-300. ISBN: 978-1-60511-096-7.

Torres, E. (2011): Geochemical processes at the C-steel / bentonite interface in a Deep Geological Repository: experimental approach and modeling. PhD Thesis. Universidad Complutense de Madrid. June 2011.

Turrero, M.J., Peña, J., Fernández, A.M., Gómez, P., Garralón, A. (2001): Porewater geochemistry and modeling within Oligocene-Miocene Clays of North-Central Spain. Proceedings of the tenth international symposium on Water-Rock Interaction. R. Cidu (ed.). ISBN 90-2651-835-8. Vol.1: 213-216. Balkema, Rotterdam.

Turrero, M.J., Fernández, A.M., Peña, J., Sánchez, M.D., Wersin, P., Bossart, P., Sánchez, M., Melón, A., Yllera, A., Garralón, A., Gómez, P., Hernán P. (2006): The pore water geochemistry of Paleogene continental mudrocks in Spain and Jurassic marine mudrocks in Switzerland: sampling methods and geochemical interpretation. Journal of Iberian Geology 32(2): 233-258.

Turrero, M.J., Escribano, A., Torres, E., Martín, P.L. (2007): Concrete/FEBEX bentonite interaction: preliminary results on short-term column experiments. 3rd International Meeting on Clays in natural and engineered barriers for radioactive waste confinement. Lille, Francia.

Villar, M.V. (Ed.), 2006b. FEBEX Project Final report. Post-mortem bentonite analysis. Publicación Técnica ENRESA 05-1/2006, Madrid, 183 pp.

Villar, M.V., Fernández, A.M., Martín, P.L., Barcala, J.M., Gómez-Espina, R., Rivas, P. (2008): Effect of heating/hydration on compacted bentonite: tests in 60-cm long cells. CIEMAT Editorial. Madrid, Spain. 72 pp.

Villar, M.V., Gómez-Espina, R. and Martín, P.L. (2006a). Behaviour of MX-80 Bentonite at Unsaturated Conditions and Under Thermo-Hydraulic Gradient . Work Performed by CIEMAT in the Context of the TBT Project. CIEMAT Technical Report CIEMAT/DIAE/M2146/1/06v1. CIEMAT, Madrid, Spain. 45 pp.

Villar, M.V., Cuevas, J., Martín P.L. (1996): Effects of heat/water flow interaction on compacted bentonite. Preliminary results. Engineering Geology 41: 257-267.

Villar, M.V., Martín, P.L., Barcala, J.M. (2005): Infiltration tests at isothermal conditions and under thermal gradient. CIEMAT Technical Report CIEMAT/DMA/M2140/1/05. CIEMAT, Madrid, Spain. 25 pp.

Wilson J., Savage D., Cuadros J., Shibata M., Ragnarsdottir K.V. (2006): The effect of iron on bentonite stability I. Background and thermodynamic considerations. Geochimica et Cosmochimica Acta 70: 306-322.